The Astrophysical Journal, 603:265–282, 2004 March 1

BARE QUARK STARS OR NAKED NEUTRON STARS? THE CASE OF RX J1856.5−3754

Roberto Turolla,[1] Silvia Zane,[2] and Jeremy J. Drake[3]
Received 2002 September 27; accepted 2003 August 15

ABSTRACT

In a cool neutron star ($T \lesssim 10^6$ K) endowed with a rather high magnetic field ($B \gtrsim 10^{13}$ G), a phase transition may occur in the outermost layers. As a consequence, the neutron star becomes "bare," i.e., no gaseous atmosphere sits on the top of the crust. The surface of a cooling, bare neutron star does not necessarily emit a blackbody spectrum because the emissivity is strongly suppressed at energies below the electron plasma frequency, ω_p. Since $\omega_p \approx 1$ keV under the conditions typical of the dense electron gas in the condensate, the emission from a $T \sim 100$ eV bare neutron star will be substantially depressed with respect to that of a perfect Planckian radiator at most energies. Here we present a detailed analysis of the emission properties of a bare neutron star. In particular, we derive the surface emissivity for an Fe composition in a range of magnetic fields and temperatures representative of cooling isolated neutron stars, like RX J1856.5−3754. We find that the emitted spectrum is strongly dependent on the electron conductivity in the solid surface layers. In the cold electron gas approximation (no electron-lattice interactions), the spectrum turns out to be a featureless depressed blackbody in the 0.1–2 keV band with a steeper low-energy distribution. When damping effects due to collisions between electrons and the ion lattice (mainly due to electron-phonon interactions) are accounted for, the spectrum is more depressed at low energies and spectral features may be present, depending on the magnetic field strength. Details of the emitted spectrum are found, however, to be strongly dependent on the assumed treatment of the transition from the external vacuum to the metallic surface. The implications of our results for RX J1856.5−3754 and other isolated neutron stars are discussed.

Subject headings: radiative transfer — stars: individual (RX J0720.4−3125, RX J1856.5−3754) — stars: neutron — X-rays: stars

1. INTRODUCTION

More than 20 X-ray sources currently associated with isolated neutron stars (INSs) show evidence for a thermal component in their spectrum, in many cases superimposed on a power-law high-energy tail. In the commonly accepted picture the hard tail is produced by nonthermal processes in the stellar magnetosphere. On the contrary, the thermal component originates at the surface, while the star cools down and internal energy is progressively radiated away. Since these objects are not complicated by strong accretion signatures, detailed observations of their thermal component provide a powerful tool to investigate directly the properties of the neutron star (NS). If the thermal emission originates in the NS atmosphere, the detection or absence of spectral lines and edges may constrain the chemical composition and/or magnetic field through a comparison with computed models (see, e.g., Shibanov et al. 1992; Rajagopal, Romani, & Miller 1997; Pons et al. 2002). Furthermore, empirical insights may be derived for the NS mass, radius, and equation of state (EOS; e.g., Lattimer & Prakash 2001).

The family of thermally emitting INSs includes seven peculiar objects serendipitously discovered in *ROSAT* PSPC pointings (see, e.g., Treves et al. 2000 and Motch 2001 for reviews; Zampieri et al. 2001). These sources (hereafter referred to as *ROSAT* INSs) are characterized by remarkably similar properties, among which are a soft, thermal spectrum with $kT \sim 100$ eV; low X-ray luminosity, $L_X \approx 10^{30}$–10^{31} ergs s^{-1}, and low column density, $N_H \sim 10^{20}$ cm^{-2}; no association with a supernova remnant; and pulsations in the 5–20 s range (detected in four sources so far). Until recently the spectral properties of the seven *ROSAT* INSs were not known in detail. PSPC observations provided evidence that a blackbody spectrum gives a satisfactory description of the data in all cases. However, the scanty statistics prevented definite conclusions from being drawn about the X-ray spectral energy distribution (SED) and did not allow for the detection of spectral features. While this situation has not yet improved for the fainter sources, the two brightest *ROSAT* INSs, RX J1856.5−3754 and RX J0720.4−3125, have been the target of deep observations with *Chandra* and *XMM-Newton*. RX J0720.4−3125 was observed with *XMM-Newton* for the first time in 2000 May, in a 62.5 ks pointing (Paerels et al. 2001; Cropper et al. 2001). The EPIC PN spectrum is well represented by a blackbody, and no spectral features have been detected, apart from variations in the column density with pulse phase that may be explained in terms of energy-dependent beaming effects or cyclotron absorption (Paerels et al. 2001; Cropper et al. 2001; Haberl et al. 2003). The X-ray flux shows a modulation with a period of 8.31 s and a pulsed fraction of ∼15% (Haberl et al. 1997; Cropper et al. 2001). Using *ROSAT* and *XMM-Newton* data, Zane et al. (2002) were able to derive the period derivative ($\dot{P} \sim 5 \times 10^{-14}$ s s^{-1}), which, when interpreted in terms of magnetodipolar braking, implies a surface magnetic field of $\sim 2 \times 10^{13}$ G. The case of RX J1856.5−3754 is even more striking. A 50 ks *Chandra* LETGS observation has convincingly shown that RX J1856.5−3754 appears to have a featureless X-ray continuum, for which a simple blackbody yields a better fit than more sophisticated atmosphere models (Burwitz et al. 2001).

[1] Department of Physics, University of Padova, via Marzolo 8, 35131 Padua, Italy; turolla@pd.infn.it.
[2] Mullard Space Science Laboratory, University College London, Holmbury St. Mary, Dorking, Surrey RH5 6NT, UK; sz@mssl.ucl.ac.uk.
[3] Smithsonian Astrophysical Observatory, Harvard-Smithsonian Center for Astrophysics, MS 3, 60 Garden Street, Cambridge, MA 02138; jdrake@head-cfa.harvard.edu.

Analysis of a very long ($\sim$500 ks) *Chandra* observation obtained in 2001 October further reinforces this conclusion and rules out the presence of strong spectral features (Drake et al. 2002). However, the presence of broadband departures from a pure blackbody spectrum has been claimed by Burwitz et al. (2003) in both *XMM-Newton* and *Chandra* data. No X-ray pulsations have been detected, and the upper limit on the pulsed fraction is now down to $\lesssim$1.3% (Ransom, Gaensler, & Slane 2002; Drake et al. 2002; Burwitz et al. 2003). RX J1856.5−3754 was the first source in this class for which an optical counterpart has been found (Walter & Matthews 1997; van Kerkwijk & Kulkarni 2001a). When used in conjunction with *Chandra* data, the recently measured star distance (about 120 pc; Kaplan, van Kerkwijk, & Anderson 2002; Walter & Lattimer 2002) yields a radiation radius of only $\sim$5–6 km (Drake et al. 2002). Very recently Haberl et al. (2003) reported the discovery of spectral feature(s) in the EPIC RGS data of RBS 1223. The feature, seemingly present also in *Chandra* data, is a deficit of counts with respect to the best-fitting blackbody at an energy of $\sim$0.2–0.3 keV and is quite broad. Its nature is still uncertain, but it could be a proton cyclotron absorption line in a magnetic field $\sim 4 \times 10^{13}$ G, as discussed by Haberl et al. (2003).

The small apparent radius and the blackbody X-ray spectrum led to the intriguing suggestion that RX J1856.5−3754 might be a strange quark star (Drake et al. 2002; Xu 2002). One of the motivations for such a claim is that bare quark stars, i.e., those not covered by a layer of hadronic matter, do not have an atmosphere and would *presumably* emit a pure blackbody spectrum (as suggested, for instance, by Xu 2002). However, further investigations are definitely needed to assess the spectral properties of these objects. While a quark star may be a conceivable option (see, however, Thoma, Trümper, & Burwitz 2003), present observations of RX J1856.5−3754 do not necessarily demand this solution and more conventional scenarios involving a NS are certainly possible. NS models based on a two-temperature surface distribution can account for both the X-ray and optical emission of RX J1856.5−3754, giving at the same time acceptable values for the stellar radius (Pons et al. 2002; Walter & Lattimer 2002; Braje & Romani 2002). However, the problem of producing a featureless spectrum from a NS has not been consistently solved yet, although possible ways to suppress the spectral features that are expected in optically thick atmospheric models have been outlined (see, e.g., Braje & Romani 2002).

In this paper we consider an alternative explanation for the peculiar X-ray spectrum of RX J1856.5−3754. In the 1970s it was commonly accepted that radiation emitted by NSs came directly from their solid surface (e.g., Brinkmann 1980, hereafter B80, and references therein). Later, the role of the thin gaseous layer that covers the star crust in shaping the emergent radiation spectrum was appreciated and model atmospheres became the standard tool for interpreting the observed emission from isolated NSs. However, highly magnetized NSs may be left without an atmosphere if they are cool enough. The reason for this is the onset of a phase transition that turns the gaseous atmosphere into a solid when the surface temperature drops below a critical temperature $T_{\rm crit}$, which, for a given chemical composition, depends on the stellar magnetic field (see Lai & Salpeter 1997; and Lai 2001 for a recent review). The determination of $T_{\rm crit}$ is still uncertain, and, in particular, only preliminary calculations are presently available for heavy-element (such as Fe) surface compositions (Lai 2001 and references therein). In § 2 we show that, given the large uncertainties on the conditions for Fe condensation, it is possible that RX J1856.5−3754 and (marginally) RX J0720.4−3125 have surface temperatures below the critical value and may be then "naked" or "bare" NSs.

The idea that RX J1856.5−3754 might be a solid-surface NS was suggested earlier by Burwitz et al. (2001) and Zane, Turolla, & Drake (2004; see also Burwitz et al. 2003). As first discussed by Lenzen & Trümper (1978), a severe reduction in the NS surface emissivity occurs at energies below the electron plasma frequency. Under the conditions for which a *ROSAT* INS is bare ($T \lesssim 100$ eV, $B \gtrsim 10^{13}$ G), the plasma frequency in the surface layers corresponds to energies $\gtrsim$1 keV (see § 2), so the NS is expected to radiate less efficiently than a blackbody emitter at soft X-ray energies and below. This is of great potential importance, since it might help reconcile the observed radiation radius with current theoretical predictions of NS radii. Furthermore, it may hold the key for explaining the featureless blackbody spectrum observed in some of these sources. In § 3 we address in detail the question of the nature of the surface emissivity of a bare NS with a pure Fe composition. The method we use is similar to that employed by B80, who was the first to investigate this issue in connection with X-ray pulsars. We found that the emissivity, and hence the shape of the emitted spectrum, depends crucially on the conductivity of the star crust. In § 3.1 we analyze a simple (albeit unrealistic) model in which only the contribution of a cold electron plasma to the dielectric tensor in the star interior is accounted for. Results for this case are qualitatively similar to those of B80. Proper account for the damping produced by interactions of (degenerate) electrons with the ion lattice (mainly through electron-phonon collisions; e.g., Potekhin 1999), however, introduces qualitative changes to the above picture, as is discussed in § 3.2. The relevance of our model to RX J1856.5−3754 is finally discussed in § 4.

2. BARE NEUTRON STARS

In this section we explore the possibility that some of the cooler INSs ($T \lesssim 100$ eV) are left without an atmosphere by a phase transition in the surface layers at large magnetic fields ($B \gtrsim 10^{13}$ G). We point out that, although this is unlikely for a light-element (H, He) composition, it might be the case for heavy elements (such as Fe), at least for some sources, notably including RX J1856.5−3754. If indeed some INSs are bare, the question of the nature of their emitted spectrum arises. In a NS with metallic surface layers (here and in the following Z and A denote the atomic number and weight of the constituent element, respectively) the density at zero pressure is given by (e.g., Lai 2001)

$$\rho_s \approx 560 A Z^{-3/5} B_{12}^{6/5} \ \mathrm{g\ cm^{-3}}, \tag{1}$$

where $B_{12} = B/10^{12}$ G. The electron plasma frequency is then

$$\hbar\omega_p = \hbar\sqrt{\frac{4\pi e^2 n_e}{m_e}} \approx 0.7 Z^{1/5} B_{12}^{3/5} \left(\frac{\rho}{\rho_s}\right)^{1/2} \ \mathrm{keV}, \tag{2}$$

where n_e is the electron density. In the following we take as a reference value for the plasma frequency that given by equation (2) with $\rho = \rho_s$ and $Z = 26$; $\omega_{p,0}$ represents then the plasma frequency in a pure iron medium with density ρ_s assuming that all electrons are in the conduction zone (see § 3.1 for a further discussion).

Cool NSs ($T \lesssim 100$ eV) emit most of their thermal radiation below the plasma frequency, and substantial deviations from a pure blackbody spectrum are expected as a result of the large absorption at $\omega \lesssim \omega_p$. Spectral features should also appear around the electron cyclotron frequency at

$$\hbar\omega_B = \frac{eB}{m_e c} \simeq 11.6 B_{12} \text{ keV}, \tag{3}$$

but, since we focus on field values $B \gtrsim 10^{13}$ G, these fall well outside the X-ray range accessible to the *Chandra* LETGS and *XMM-Newton* EPIC PN and are of no immediate interest.

The properties of atoms and condensed matter are qualitatively changed by magnetic effects when $b = B/B_0 \gg 1$, $B_0 = m_e e^3 c/\hbar^3 \simeq 2.35 \times 10^9$ G. Theoretical research on matter in superstrong fields started over 40 years ago, and although many uncertainties still remain, much progress has been made, especially for H and He compositions (see Lai 2001 and references therein). In particular, when $b \gg 1$, electrons are strongly confined in the direction perpendicular to the magnetic field and atoms attain a cylindrical shape. Moreover, it is possible for these elongated atoms to form molecular chains by covalent bonding along the field direction. Interactions between the linear chains can then lead to the formation of three-dimensional condensates. As discussed by Lai & Salpeter (1997) and Lai (2001), in the case of hydrogen the infinite linear chains (and metallic hydrogen) are certainly bound, favoring the possibility of condensation for sufficiently low temperatures and/or strong magnetic fields. The critical temperature below which phase separation between condensed H and vapor occurs is

$$T_{\rm crit}^{\rm H} \approx 0.1 Q_\infty, \tag{4}$$

with

$$Q_\infty \approx 194.1 B_{12}^{0.37} - 4.4(\ln B_{12} - 6.05)^2 - \hbar\omega_{p,p} - \frac{\hbar}{2}\left(\omega_{B,p}^2 + \omega_{p,p}^2\right)^{1/2} + \frac{1}{2}\hbar\omega_{B,p} \text{ eV}, \tag{5}$$

where $\omega_{p,p}$ and $\omega_{B,p}$ are the proton plasma and cyclotron frequencies, respectively.

For heavier elements (such as Fe), the lattice structure and the cohesive properties of the condensed state are very uncertain and are different from those of H and He. For instance, unless the field is extremely high ($B_{12} \gg 100$), it is likely that the linear chains are unbound for $Z \gtrsim 6$. More recent computations of the cohesive energy Q_s of the three-dimensional condensate showed that Q_s is only a tiny fraction ($\sim$0.5%) of the atomic binding energy, correcting earlier overestimates (Jones 1986; see also Neuhauser, Koonin, & Langanke 1987):

$$Q_s \lesssim 0.05|E_{\rm atom}| \sim Z^{9/5} B_{12}^{2/5} \text{ eV} \quad \text{for } Z \gtrsim 10. \tag{6}$$

On the other hand (see again Lai 2001), even such a weak cohesion of the Fe condensate can give rise to a phase transition at sufficiently low T. The critical temperature at which phase separation occurs can be estimated by equating the ion density of the condensed phase near zero pressure (eq. [1]) to the gas density in the vapor (Lai 2001),

$$\rho_g \approx 390 A^{5/2} T^{5/2} \exp\left(-\frac{Q_s}{T}\right) \text{ g cm}^{-3}. \tag{7}$$

This gives

$$T_{\rm crit}^{\rm Fe} \lesssim 0.1 Q_s \approx 27 B_{12}^{2/5} \text{ eV}. \tag{8}$$

It should be noted that, although representing the more recent available estimates, these expressions for heavier elements are still quite crude: all models are approximate near zero pressure and the structure itself of the lattice is very uncertain. For our purposes, they should be regarded as being typically accurate to an order of magnitude. In addition, the vapor density becomes much less than the condensation density and a phase transition is unavoidable only when the temperature drops below $\sim T_{\rm crit}/2$ (see Lai 2001).

The critical condensation temperatures for H and Fe are plotted as a function of B in Figure 1. The filled circles show the position in the B-T plane of the coolest ($T \lesssim 100$ eV), thermally emitting INSs for which an estimate of the magnetic field is available (see Table 1). We have also included RX J1856.5−3754 in Figure 1; its position is indicated by a horizontal line since its magnetic field is not presently known. In order to obtain the local surface temperature, i.e., the quantity reported in Figure 1, a gravitational redshift correction was applied to the values listed in Table 1, according to the expression $T_{\rm surf} = (1+z)T_{\rm bb}$, where $(1+z)^{-1} = (1 - 2GM/c^2R)^{1/2} \simeq 0.8$ (M and R are the star mass and radius, respectively). Here $T_{\rm bb}$ is the color temperature, as derived from the blackbody fit.

It is apparent from Figure 1 that all INSs have a temperature well in excess of the H critical temperature: if surface layers are H dominated, the presence of a gaseous atmosphere is unavoidable. On the other hand, if INSs have not accreted much gas, one might

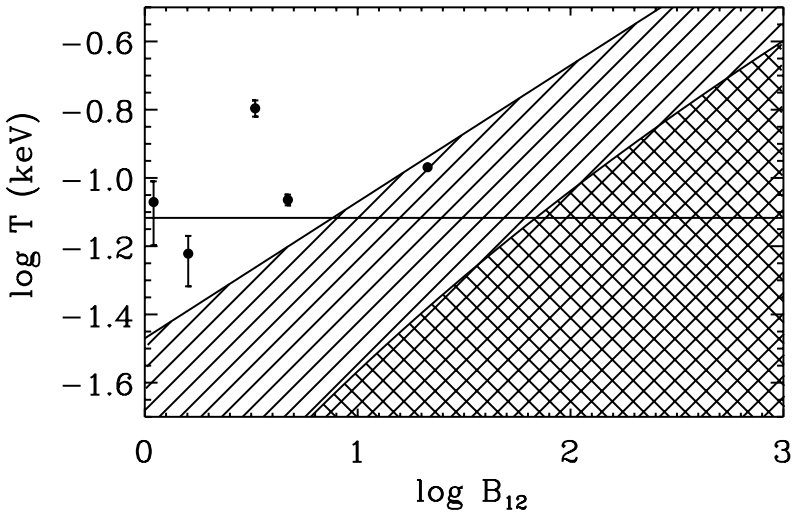

FIG. 1.—Critical temperature for H and Fe as a function of the magnetic field. Condensation is possible in the hatched region for Fe and in the cross-hatched region for H. The filled circles with error bars mark the position of five cool INSs (see Table 1). The horizontal line is drawn in correspondence to the color temperature of RX J1856.5−3754.

expect to detect thermal emission directly from the iron surface layers. If this is the case, the outermost layers of RX J1856.5−3754 (depending on the magnetic field), and possibly RX J0720.4−3125, might be in the form of hot condensed matter, in which case the usual radiative transfer computations do not apply.

3. THE SURFACE EMISSIVITY

The emission properties of the NS surface have been first analyzed by Lenzen & Trümper (1978) and in some more detail by B80. Both of these works were aimed to X-ray pulsars, where the surface temperature is a few keV, and treated the medium inside the star as a cold electron plasma, neglecting all possible effects due to electron degeneracy and ion lattice (primarily through electron-phonon interactions). The (constant) damping frequency that appears in B80 calculations is mainly used to smear the resonance at the cyclotron frequency. Moreover, birefringence in the magnetized vacuum outside the star was not accounted for. In this section we derive the NS surface emissivity following an approach similar to that discussed in B80. To better illustrate the importance of electron-phonon interactions, we first consider a pure cold electron plasma, repeating Brinkmann's calculation for the parameter values appropriate to cold isolated NSs (§ 3.1). A complete treatment that includes the polarization properties of magnetized vacuum is presented in the Appendix. Since, as we show there, this more general approach is quite cumbersome and only gives tiny differences with respect to the simpler one based on unpolarized radiation, the latter is used below. In § 3.2 we analyze the more realistic case in which the damping of electromagnetic waves produced by the presence of the ion lattice is included.

3.1. *The Cold Plasma Case*

We start considering the medium inside the star as a cold electron plasma and neglect the damping of free electrons due to collisions. We introduce a Cartesian frame as in B80 (see his Figs. 1 and 2) with the z-axis parallel to the surface normal. The

TABLE 1
ISOLATED NEUTRON STAR PARAMETERS

Source	T_{bb}[a] (eV)	B[b] (10^{12} G)	References
RX J1856.5−3754	61.1 ± 0.3	...	1, 2
RX J0720.4−3125	86.0 ± 0.6	21.3 ± 0.1	3, 4
Vela	128.4 ± 7	3.3	5, 6
Geminga	$48.3^{+6.1}_{-9.5}$	1.5	7, 8
PSR 0656+14	69.0 ± 2.5	4.7	9, 6
PSR 1055−52	$68.1^{+10.2}_{-17.2}$	1.1	10, 6

[a] Errors refer to 2 σ confidence level.
[b] As computed from the spin-down formula; period derivative is very accurate for the three radio pulsars and for Geminga. Errors refer to 90% confidence level for RX J0720.4−3125.

REFERENCES.—(1) Burwitz et al. 2001; (2) Drake et al. 2002; (3) Paerels et al. 2001; (4) Zane et al. 2002; (5) Pavlov et al. 2001; (6) Taylor, Manchester, & Lyne 1993; (7) Halpern & Wang 1997; (8) Bignami & Caraveo 1996; (9) Marshall & Schulz 2002; (10) Greiveldinger et al. 1996.

direction of the incident wavevector $\boldsymbol{k}$ is specified by the angle of incidence i and the azimuth β. The magnetic field direction $\boldsymbol{b} \equiv \boldsymbol{B}/B$ is at an angle α with respect to the z-axis, and $\boldsymbol{b}$ lies in the x-z plane. Given a star surface element $dA = 2\pi R^2 \sin\theta\, d\theta$ at magnetic colatitude θ, we first compute the total reflectivity ρ_ω of the surface for incident unpolarized radiation. Then, since the absorption coefficient is simply $\alpha_\omega = 1 - \rho_\omega$, Kirchhoff's law yields the emissivity $j_\omega = \alpha_\omega B_\omega(T)$, where T is the temperature of the emitting element. In general, ρ_ω depends on the direction of the refracted ray (see below). Therefore, the monochromatic flux f_ω emitted by the surface element must be computed by integrating over all incident directions,

$$f_\omega = \int_0^{2\pi} \int_{-\pi/2}^{\pi/2} j_\omega(i, \beta, \theta) \sin i\, di\, d\beta. \tag{9}$$

The flux emitted by the entire surface is given by[4]

$$F_\omega = \frac{1}{4\pi R^2} \int_{\text{sphere}} f_\omega\, dA = \frac{1}{2} \int_0^{\pi} \sin\theta\, d\theta \int_0^{2\pi} \int_{-\pi/2}^{\pi/2} j_\omega(i, \beta, \theta) \sin i\, di\, d\beta. \tag{10}$$

At the surface, an incident electromagnetic wave, described by its electric field $\boldsymbol{E}$ and wavevector $\boldsymbol{k}$, is partly reflected ($\boldsymbol{E}''$, $\boldsymbol{k}''$) and partly refracted. As a result of the birefringence of the medium, the refracted wave is the sum of an ordinary ($\boldsymbol{E}_1'$, $\boldsymbol{k}_1'$) and an extraordinary ($\boldsymbol{E}_2'$, $\boldsymbol{k}_2'$) mode. In order to compute the reflectivity, we need to solve the dispersion relation and compute the refractive index n for the two modes of propagation. In our frame, the dielectric tensor for a cold electron plasma is given by

$$\epsilon_{ij} = \begin{pmatrix} S\cos^2\alpha + P\sin^2\alpha & -iD\cos\alpha & \sin\alpha\cos\alpha(P - S) \\ iD\cos\alpha & S & -iD\sin\alpha \\ \sin\alpha\cos\alpha(P - S) & iD\sin\alpha & P\cos^2\alpha + S\sin^2\alpha \end{pmatrix}, \tag{11}$$

with

$$\begin{pmatrix} R \\ L \end{pmatrix} = 1 - \frac{\omega_p^2}{\omega^2} \frac{\omega}{\omega \mp \omega_B}, \tag{12}$$

$$P = 1 - \frac{\omega_p^2}{\omega^2}, \tag{13}$$

$$\begin{pmatrix} S \\ D \end{pmatrix} = \frac{R \pm L}{2}. \tag{14}$$

By introducing the Maxwell tensor $\lambda_{ij} = k_i' k_j' - k'^2 \delta_{ij} + (\omega^2/c^2)\epsilon_{ij}$, where k_i' are the Cartesian components of $\boldsymbol{k}'$ and $k'^2 \equiv k_i' k_i'$, the dispersion relation is obtained by imposing $|\lambda_{ij}| = 0$. For our purposes it is convenient to write the resulting expression in terms of angle of incidence i and the (complex) refractive index $n = k'c/\omega$. By using an expression formally analogous to Snell's law $n = \sin i / \sin\Theta$ (where now Θ is a complex quantity that replaces the angle of refraction while i is real; see, e.g., Marion 1965), it is

$$n^4\left(P + v\sin^2\alpha\right) + n^2\left(gv - 2PS + u\sin^2\alpha\right) + PRL + gu = \sin i \sin(2\alpha)\cos\beta\left(n^2 - \sin^2 i\right)^{1/2}\left(u + n^2 v\right). \tag{15}$$

In the previous expression $v = S - P$, $u = PS - RL$, and $g = \sin^2 i[1 - \sin^2\alpha(1 + \cos^2\beta)]$. Squaring equation (15) gives a fourth-order polynomial equation in n^2 that can be solved analytically. Clearly only two out of four solutions satisfy the original dispersion relation and represent the refractive indexes for the two propagation modes in the magnetized plasma, n_m, $m = 1, 2$. As noted by B80, the only practical way of finding the two meaningful roots is to substitute them back into equation (15) and check numerically the residual. This, however, turned out to be troublesome for some values of the parameters, as we discuss later on. For $i = 0$, $\alpha = 0$ or $\pi/2$, $\beta = \pi/2$ or $3\pi/2$, the right-hand side of equation (15) vanishes, and the dispersion relation reduces to a quadratic equation in n^2, which is then solved instead of the quartic.

[4] Viewing angle effects have been neglected in evaluating the flux from eq. (10).

Once the refractive indexes are known, we can solve the wave equation for the two refracted modes $\lambda_{ij}(n_m)E'_{m,j}=0$, where $E'_{m,j}$ are the Cartesian components of $\boldsymbol{E}'_m$, obtaining the two ratios $E'_{m,x}/E'_{m,z}$ and $E'_{m,y}/E'_{m,z}$. We performed the calculation (double-checked with the aid of an algebraic manipulator), obtaining

$$\begin{aligned}\frac{E'_{m,x}}{E'_{m,z}} \equiv a_m = &\Bigg[-n_m^2 \sin^2 i \sin\beta\cos\beta - iD\sin^2 i\cos\alpha + iD\cos\beta\sin\alpha\,\sin i\sqrt{n_m^2 - \sin^2 i}\\ &- \sin\beta(P-S)\sin\alpha\cos\alpha\,\sin i\sqrt{n_m^2-\sin^2 i} + \sin^2 i\sin\beta\cos\beta\big(P\cos^2\alpha + S\sin^2\alpha\big) + iD\cos\alpha P\Bigg]\\ &\times\Bigg\{-n_m^2\sin i\sqrt{n_m^2-\sin^2 i}\sin\beta + iD\sin\alpha n_m^2 - iD\sin\alpha\,\sin^2 i\cos^2\beta - iD\cos\alpha\,\cos\beta\sin i\sqrt{n_m^2-\sin^2 i}\\ &+ \sin i\sqrt{n_m^2-\sin^2 i}\big[\sin\beta S + \sin\beta\sin^2\alpha(P-S)\big] - (P-S)\sin\alpha\cos\alpha\,\sin^2 i\sin\beta\cos\beta - iD\sin\alpha P\Bigg\}^{-1},\\ \frac{E'_{m,y}}{E'_{m,z}} \equiv b_m = &\Big[a_m\big(\sin^2 i\sin\beta\cos\beta - iD\cos\alpha\big) + \sin\beta\sin i\sqrt{n_m^2-\sin^2 i} + iD\sin\alpha\Big]\times\big(\sin^2\beta\sin^2 i - n_m^2 + S\big)^{-1}. \end{aligned} \tag{16}$$

While the previous expression for b_m agrees with that given in B80, our result for a_m is different and we were unable to recover his expression.

The ratios in equation (16) are then inserted into the Fresnel equations that fix the boundary conditions at the interface between the two media (see Jackson 1975 and eqs. [17] and [18] in B80). This allows the derivation of the components of the electric field of the reflected wave parallel and perpendicular to the plane of incidence ($E''_\parallel$ and $E''_\perp$) in terms of the same components of the incident wave ($E_\parallel$ and $E_\perp$). We rederived the expressions given in B80 and found

$$\begin{aligned} E''_\parallel &= \mathcal{D}^{-1}\left[\frac{A_+B_- - A_-B_+}{\mathcal{B}_1\mathcal{B}_2(1+w_2)(1+w_1)}E_\perp + (A_- - B_-)E_\parallel\right],\\ E''_\perp &= \mathcal{D}^{-1}\left[\left(\frac{1-w_1}{1+w_1}A_+ - \frac{1-w_2}{1+w_2}B_+\right)E_\perp + 2\mathcal{B}_1\mathcal{B}_2(w_1-w_2)E_\parallel\right], \end{aligned} \tag{17}$$

where

$$\begin{aligned} A_\pm &= \mathcal{B}_1(1+w_1)\left[\mathcal{A}_2\left(w_2\cos i \pm \frac{1}{\cos i}\right) + \sin i\right],\\ B_\pm &= \mathcal{B}_2(1+w_2)\left[\mathcal{A}_1\left(w_1\cos i \pm \frac{1}{\cos i}\right) + \sin i\right], \end{aligned} \tag{18}$$

$w_m = (n_m^2 - \sin^2 i)^{1/2}/\cos i$, $\mathcal{A}_m = b_m\sin\beta - a_m\cos\beta$, $\mathcal{B}_m = b_m\cos\beta + a_m\sin\beta$, and $\mathcal{D} = A_+ - B_+$. These expressions were double-checked with the aid of an algebraic manipulator and differ again from those in B80; we also note that our definition of $B_\pm$ is different from that of B80.

The reflection coefficient for unpolarized radiation can be expressed as the combination of the reflectivity of parallel and perpendicularly polarized incident waves, $\rho_\omega = (\rho_{\parallel,\omega} + \rho_{\perp,\omega})/2$. Since the reflectivity is defined as the ratio of the reflected to the incident wave amplitudes, $\rho_{\parallel,\omega}$ is the sum of the square moduli of the coefficients of $E_\parallel$ in equation (17). Similarly, $\rho_{\perp,\omega}$ is obtained by adding together the square moduli of the coefficients of $E_\perp$.

The absorption coefficient $\alpha_\omega = 1 - \rho_\omega$ has been computed numerically in the relevant angular ranges following the procedure outlined above, and the results have been used to evaluate the integral in equation (9). Although the numerical scheme is rather straightforward, care should be used since the refractive index becomes resonant where the coefficient of the higher order term in equation (15) vanishes (B80; see also Melrose 1986). This happens at $P + v\sin^2\alpha = 0$, that is to say, at the two frequencies

$$\omega_\pm^2 = \frac{\omega_p^2 + \omega_B^2}{2}\left\{1 \pm \left[1 - \frac{4\omega_p^2\omega_B^2\cos\alpha}{\left(\omega_p^2+\omega_B^2\right)^2}\right]^{1/2}\right\}. \tag{19}$$

Assuming no collisional damping has the main advantage that the fourth-order polynomial obtained by squaring the dispersion relation has real coefficients and its roots are either real or complex conjugates in pairs. Numerical experimenting shows that the roots develop an imaginary part only close to the resonances and are real and distinct otherwise. As discussed by Melrose (1986), there exist two cutoff energies at which one of the two indexes vanishes. The cutoff energies are α dependent, and the smallest one, ω_0, falls in the range $\omega_- < \omega_0 < \omega_+$. This corresponds to the appearance of an evanescent mode, which cannot propagate into the medium. Modes for which the refractive index has a large imaginary part are severely damped (e.g., Jackson 1975), so they cannot penetrate much below the surface either. We point out that the existence of these damped waves is not in contradiction with having

neglected collisional damping. The "conductivity" $\sigma_{ij}^{\rm pl}$ of a cold plasma can be computed from the dielectric tensor given by equation (11) using the standard relation

$$\epsilon_{ij} = \delta_{ij} + i\frac{4\pi}{\omega}\sigma_{ij}^{\rm pl} \tag{20}$$

and is therefore purely imaginary (see Jackson 1975; Mészáros 1992). Quotation marks are placed on "conductivity" because there is no resistive loss of energy in this case. Yet, depending on their frequency and grazing angle, electromagnetic waves may be exponentially damped in the cold electron plasma.

In all cases in which one of the acceptable roots is real and negative or it is complex and its imaginary part exceeds a given value, only one refracted mode survives. Consequently, we adopt a "one-mode" description to derive the reflectivity. By specializing the previous calculation to a single mode (labeled "1" for convenience) and defining $\mathcal{C}_1 = \epsilon_{31}a_1 + \epsilon_{32}b_1 + \epsilon_{33}$, we obtain (see also Jackson 1975)

$$E_{\parallel}'' = \frac{\mathcal{C}_1 \arctan i - \mathcal{A}_1}{\mathcal{C}_1 \arctan i + \mathcal{A}_1}E_{\parallel}, \qquad E_{\perp}'' = \frac{\sqrt{n_1^2 - \sin^2 i} - \cos i}{\sqrt{n_1^2 - \sin^2 i} + \cos i}E_{\perp}, \tag{21}$$

from which the reflectivity follows.

As we mentioned earlier, selecting the two relevant roots of the fourth-order polynomial may become difficult in some parameter ranges. While for most values of the energy and angles the two meaningful roots produce a residual many orders of magnitude below that of the spurious ones, in some cases all residuals are small and of the same order. We encountered situations in which, owing to round-off errors and despite the use of quadruple-precision complex arithmetic, one of the relevant roots produced a residual larger than that of the spurious solutions. A bad choice of the roots usually gives negative absorption. In these cases the calculation is repeated with a different choice of the roots until α_ω is positive and its value is close to those computed for neighboring values of the parameters.

The quantity $f_\omega/B_\omega(T)$ (see eq. [9]) is shown in Figure 2 as a function of energy for $B = 10^{12}$ G and different values of the angle α. Here the surface temperature is assumed constant. In general, the emissivity becomes lower as the magnetic field is more and more tilted with respect to the surface normal. The strong absorption around the resonant frequency ω_- is clearly seen; the absorption dip becomes more pronounced (and the surface emissivity decreases) as α approaches $\pi/2$. The total monochromatic emissivity is obtained integrating over the entire stellar surface (eq. [10]), once the magnetic field topology is specified. Here and in the following we assume that the field is dipolar, $B = B_p[(4-f)\cos^2\theta + f]^{1/2}/2$, where B_p is the polar field strength and $f \simeq 1.2$ accounts for general relativistic corrections in a Schwarzschild spacetime (see, e.g., Pavlov & Zavlin 2000). Accordingly, α is related to the magnetic colatitude θ by $\cos^2\alpha = \left\{4 - 4f/[(4-f)\cos^2\theta + f]\right\}/(4-f)$.

The quantity $F_\omega/B_\omega(T)$ is shown in Figure 3 for different values of B_p (models computed accounting for electron-phonon interactions are also shown; see § 3.2 for details). Again, the surface temperature is taken to be constant. As expected, integration over θ smears out any strong feature around ω_-, as it can be seen comparing the solid line in Figure 3 with those in Figure 2 (for $B_p > 10^{12}$ G the angle-averaged resonant feature lies outside the energy range that we have considered). Below ω_- one of the two modes is nonpropagating, a so-called whistler. Whistlers have a very large refractive index, which diverges at ω_- and for $\omega \to 0$, and this explains the high reflectivity at these frequencies (e.g., Melrose 1986). The increase of the plasma frequency with B is responsible for the lower emissivity at larger fields, and if we restrict to energies below the (angle-averaged) resonance ω_-, the dependence on energy is about the same (i.e., the curves are nearly self-similar; see again Fig. 3).

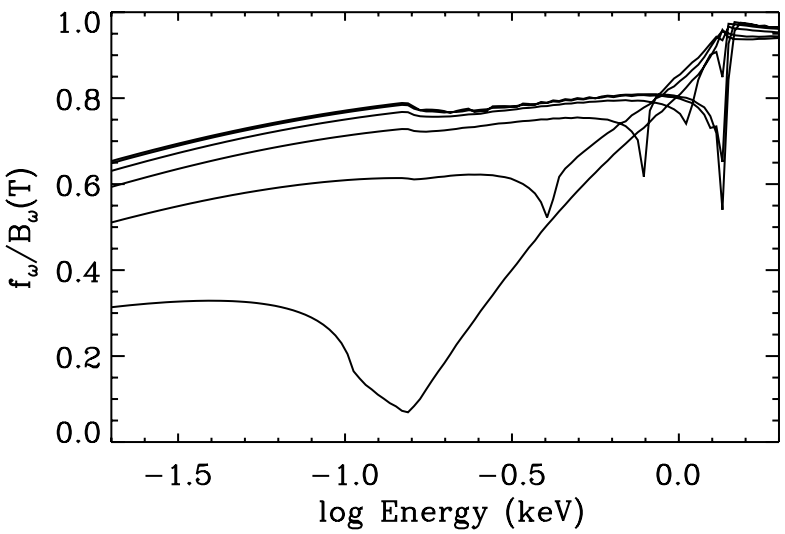

FIG. 2.—Monochromatic absorption coefficient as a function of energy for $B = 10^{12}$ G and different values of the magnetic field angle: curves represent, from top to bottom, $2\alpha/\pi = 0.05$, 0.2, 0.4, 0.6, 0.8, 0.95. The plasma frequency given by $\omega_{p,0}$ has been used here.

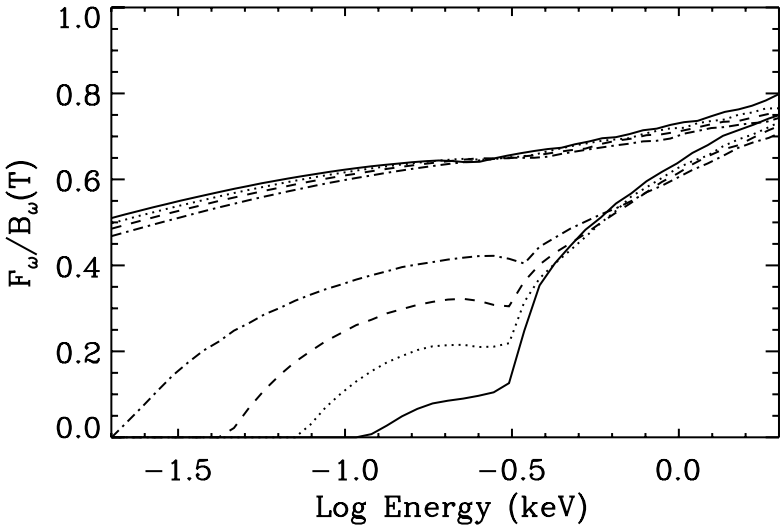

FIG. 3.—Total absorption coefficient averaged over the star surface, $F_\omega/B_\omega(T)$, as a function of energy and for different values of the magnetic field: $B_p = 5 \times 10^{12}$ G (*solid line*), 10^{13} G (*dotted line*), 2×10^{13} G (*dashed line*), and 5×10^{13} G (*dot-dashed line*). The two sets of curves correspond to models without and with electron-phonon damping accounted for (the latter are evaluated assuming $T = 10^6$ K). The plasma frequency $\omega_{p,0}$ has been used here.

The model presented so far has been computed using for the plasma frequency in the surface layers our reference value $\omega_{p,0}$. It should be stressed, however, that this value, which relies on the zero-pressure surface density given by equation (1), is just an estimate (see, e.g., Lai 2001). In order to assess the effects of this on the emitted spectrum, we explored the parameter space by varying the electron plasma frequency around $\omega_{p,0}$; this accounts also for the uncertainties on the number of free electrons per nucleon, i.e., deviations from our reference value $Z = 26$.

While the energy dependence of the absorption coefficient does not change significantly, an increase in the plasma frequency at fixed B produces an overall decrease of the emissivity. This is illustrated in Figure 4, where the ratio of the emitted to the blackbody power in the 0.1–2 keV band is plotted against the plasma frequency for $B_p = (3,\ 5) \times 10^{13}$ G. As can be seen from Figure 4, in this simple description we expect that the star surface radiates only $\sim$30% of the blackbody power if the plasma frequency (the density) is about a factor of 6 (36) higher than the estimate provided by equation (2) (eq. [1]). In addition, since in this simplified description $f_\omega/B_\omega(T)$ is found to vary with the magnetic field angle (Fig. 2), viewing effects may be relevant with even larger depression expected if the star is viewed equator-on.

3.2. *Electron-Phonon Interaction*

In the calculation presented so far all collisional damping effects have been neglected; therefore, the only source of "conductivity" is the cold plasma. This is of course an oversimplification. In the solid crust of a NS with $B \sim 10^{12}$–10^{13} G and $T \sim 10^6$ K electrons are strongly degenerate ($T \ll T_F$, where T_F is the Fermi temperature). Furthermore, if $\rho \sim \rho_s$, quantum effects due to the magnetic field are not negligible. In the degenerate surface layers charge (and heat) is transported primarily by electrons.

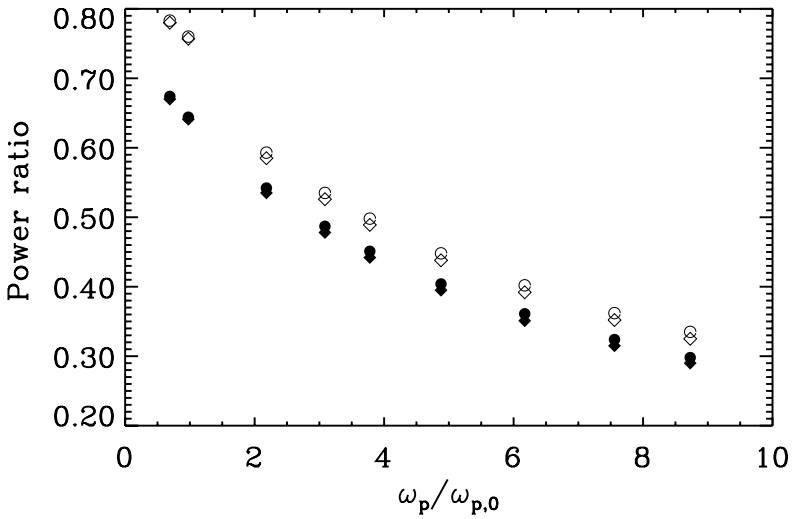

FIG. 4.—Ratio of the emitted to the blackbody power in the 0.1–2 keV band for different values of the plasma frequency. Circles refer to $B_p = 3 \times 10^{13}$ G and diamonds to $B_p = 5 \times 10^{13}$ G. Filled and open symbols are for the uniform and meridional variation temperature distributions, respectively. In the latter case we assumed a profile $T^4(\theta) = T^4_{\rm surf}[K + (4 - K)\cos^2\theta]/[1 - 0.47(1 - K)](1 + 3\cos^2\theta)$ with $K = 10^{-4}$ (e.g., Greenstein & Hartke 1983; Possenti, Mereghetti, & Colpi 1996).

Several efforts have been devoted to an accurate determination of the electrical conductivity σ, mostly because this is the basic quantity governing the magnetic field evolution (see, e.g., Flowers & Itoh 1976; Yakovlev & Urpin 1980; Potekhin 1999 and references therein). In particular, it is well known that while at temperatures above the crystallization temperature of the ions the main factor governing the electrical conductivity is scattering off ions, below the crystal melting point the dominant process is scattering by crystal lattice vibrations (phonons) through *Umklapp* processes. Eventually, if the temperature decreases further, impurities in the crystal structure and scattering off lattice defects start to be important.

Magnetic fields in the NS crust complicate electron transport, in particular, making it anisotropic (Kaminker & Yakovlev 1981; Yakovlev 1984; Hernquist 1984; Potekhin 1999). Electrons move freely parallel to $\boldsymbol{B}$, but their motion perpendicular to the field is quantized. Therefore, transport properties will be affected through the influence of the discrete spectrum on the density of states and collision times. The electrical conductivity tensor is computed from the transport tensor and can be expressed as (Hernquist 1984; Potekhin 1999)

$$\sigma_{ij} = \int e^2 \frac{N_B(\varepsilon)}{\varepsilon/c^2} \tau_{ij}(\varepsilon) \left(-\frac{\partial f_0}{\partial \varepsilon}\right) d\varepsilon, \tag{22}$$

where ε is the electron energy (including the rest energy $m_e c^2$), $f_0(\varepsilon)$ is the Fermi-Dirac distribution,

$$N_B(\varepsilon) = \frac{m_e \omega_B}{2(\pi\hbar)^2} \sum_{n=0}^{n_{\max}} g_n \left[\left(\frac{\varepsilon}{c}\right)^2 - (m_e c)^2 - 2 m_e \hbar \omega_B n \right]^{1/2}, \tag{23}$$

g_n is the statistical weight of the nth Landau level, and $n_{\max}$ is the maximum Landau number for a given energy ε (see Potekhin 1999 for all details). The quantities $\tau_{ij}(\varepsilon)$ in equation (22) play the role of relaxation times. The tensor σ_{ij} has three independent components: one parallel to the field ($\sigma_{zz} \equiv \sigma_{\parallel}$), one transverse ($\sigma_{xx} = \sigma_{yy} \equiv \sigma_{\perp}$), and one off-diagonal (Hall) component $\sigma_{xy} \equiv \sigma_{\rm H}$, which is nondissipative. In general, evaluating equation (22) requires energy integration, but for strongly degenerate electrons and not too close to the Landau thresholds this becomes unnecessary. In this case it is $\sigma_{ij} \approx (e^2 n_e c^2/\varepsilon_{\rm F}) \tau_{ij}(\varepsilon_{\rm F})$, where $\varepsilon_{\rm F}$ is the Fermi energy.

The way in which the magnetic field affects the charge transport depends on its strength. According to Potekhin et al. (2003), the nonquantizing (classical) regime occurs if $T \gg T_B$, where $kT_B = \hbar e B/(m_e c)$. Even a nonquantizing magnetic field, which essentially does not affect the thermodynamic properties of matter, hampers transverse motion and produces Hall currents. In the opposite case, $T \ll T_B$, one can distinguish between a weakly quantizing (when electrons populate several Landau levels) and a strongly quantizing regime (when the magnetic field confines most electrons in the ground Landau level). Transition to the strongly quantizing regime occurs below the first Landau threshold, i.e., for $\rho < \rho_B \approx 7 \times 10^3 (A/Z) B_{12}^{3/2}$ g cm^{-3}. Note that the zero-pressure density ρ_s is much smaller than ρ_B for $B \gg 10^{10}$ G.

So far, the most complete expressions for the electrical conductivity are those computed by Potekhin (1999), by taking into account correlation effects in the strongly coupled Coulomb liquid and multiphonon scattering in the Coulomb crystal (Baiko et al. 1998). These results show that in a weakly quantizing field the conductivity in the longitudinal and transverse direction oscillates around their classical values. However, such oscillations are quite prominent in the regime of strong quantization, where they may reach several orders of magnitudes. In this case the transport properties of the matter are very different from those in the classical regime.

In order to include effects of electron-phonon scattering in our computation, it is convenient to introduce the effective relaxation times. In the regime of strongly degenerate electrons, when thermal averaging is unimportant, the relaxation times are related to the conductivity along the various directions by $\tau_{xx} = \tau_{yy} = 4\pi\sigma_{\perp}/\omega_p^2$, $\tau_{zz} = 4\pi\sigma_{\parallel}/\omega_p^2$ (e.g., Ziman 1978; Yakovlev & Urpin 1980; Potekhin 1999). Then we proceed in a standard (although approximate) way by summing the relevant effective frequencies of the different processes. Note that while for transport along the field the effective collision frequency for electron-phonon damping is simply $\sim\tau_{\parallel}^{-1} = \tau_{zz}^{-1}$, for transport across the field it is not always $\sim\tau_{xx}^{-1}$. In the strong-field regime it becomes directly proportional to τ_{xx}. Physically this reflects the fact that the relaxation time in the transverse direction is, in the strong-field regime, longer than the time between electron-phonon collisions ($\tau_{\perp}$), which in turn determines the damping according to Heisenberg's principle. Accordingly, we derived the collision frequency from the interpolation formula by Potekhin (1999), valid at any field strength $\tau_{xx} = \tau_{\perp}/(1 + \omega_B^2 \tau_{\perp}^{-2})$.

We focus on the case $\boldsymbol{B} \parallel z$ (i.e., $\alpha = 0$) and write the conductivity tensor of the pure plasma component (eq. [20]) in rotating coordinates ($\boldsymbol{e}_+$, $\boldsymbol{e}_-$, $\boldsymbol{e}_z$), $\boldsymbol{e}_{\pm} = \boldsymbol{e}_x \pm i\boldsymbol{e}_y$ (Mészáros 1992). In this frame the conductivity tensor $\tilde{\sigma}^{\rm pl}$ is diagonal,[5]

$$\tilde{\sigma}_{ij}^{\rm pl} = \Lambda_{ik} \sigma_{kl}^{\rm pl} \Lambda_{lj}^{-1} = \frac{i\omega_p^2}{4\pi\omega} \begin{pmatrix} \dfrac{1}{1+\omega_B/\omega} & 0 & 0 \\ 0 & \dfrac{1}{1-\omega_B/\omega} & 0 \\ 0 & 0 & 1 \end{pmatrix}, \tag{24}$$

[5] The plasma polarization tensor, whose elements are directly related to the collision times, is in fact $\Pi_{ij} \equiv v^{-1}(\delta_{ij} - \epsilon_{ij}) \equiv -(i4\pi/v\omega)\sigma_{ij}$, where $v = \omega_p^2/\omega^2$. In a magnetic field and in rotating coordinates with $\boldsymbol{B} \parallel z$, the polarization tensor is diagonal (see, e.g., Mészáros 1992).

where

$$\Lambda_{ij} = \begin{pmatrix} 1 & i & 0 \\ 1 & -i & 0 \\ 0 & 0 & 1 \end{pmatrix}. \tag{25}$$

The conductivity tensor related to electron-phonon scattering can be written (again in rotating coordinates) as

$$\tilde{\sigma}_{ij}^{e\text{-ph}} = \begin{pmatrix} \sigma_\perp & 0 & 0 \\ 0 & \sigma_\perp & 0 \\ 0 & 0 & \sigma_\parallel \end{pmatrix}. \tag{26}$$

We then obtain

$$\begin{aligned} \tilde{\sigma}_{zz}^{\rm tot} &= \left(\frac{\omega_p^2}{4\pi}\right)\left[\left(\frac{4\pi\tilde{\sigma}_{zz}^{\rm pl}}{\omega_p^2}\right)^{-1} + \tau_\parallel^{-1}\right]^{-1} = \frac{i\omega_p^2}{4\pi\omega}\frac{1}{1+i\omega_\parallel^D/\omega}, \\ \tilde{\sigma}_{xx}^{\rm tot} &= \left(\frac{\omega_p^2}{4\pi}\right)\left[\left(\frac{4\pi\tilde{\sigma}_{xx}^{\rm pl}}{\omega_p^2}\right)^{-1} + \tau_\perp^{-1}\right]^{-1} = \frac{i\omega_p^2}{4\pi\omega}\frac{1}{1+\omega_B/\omega+i\omega_\perp^D/\omega}, \\ \tilde{\sigma}_{yy}^{\rm tot} &= \left(\frac{\omega_p^2}{4\pi}\right)\left[\left(\frac{4\pi\tilde{\sigma}_{yy}^{\rm pl}}{\omega_p^2}\right)^{-1} + \tau_\perp^{-1}\right]^{-1} = \frac{i\omega_p^2}{4\pi\omega}\frac{1}{1-\omega_B/\omega+i\omega_\perp^D/\omega}, \end{aligned} \tag{27}$$

where the quantities

$$\omega_\parallel^D = \frac{\omega_p^2}{4\pi\sigma_\parallel}, \qquad \omega_\perp^D = \frac{1}{2}\left(\frac{\omega_p^2}{4\pi\sigma_\perp}\right)\left[1-\sqrt{1-4\omega_B^2\left(\frac{4\pi\sigma_\perp}{\omega_p^2}\right)^2}\right] \tag{28}$$

play the role of damping frequencies in the two different directions. By transforming back to nonrotating coordinates, we finally get

$$\frac{i4\pi}{\omega}\sigma_{ij}^{\rm tot} = \frac{1}{2}\begin{pmatrix} L^{\rm tot}+R^{\rm tot}-2 & i(L^{\rm tot}-R^{\rm tot}) & 0 \\ -i(L^{\rm tot}-R^{\rm tot}) & L^{\rm tot}+R^{\rm tot}-2 & 0 \\ 0 & 0 & 2P^{\rm tot}-1 \end{pmatrix}, \tag{29}$$

from which the dielectric tensor follows as

$$\epsilon_{ij}^{\rm tot} \equiv \delta_{ij} + \frac{i4\pi}{\omega}\sigma_{ij}^{\rm tot} = \begin{pmatrix} S^{\rm tot} & -iD^{\rm tot} & 0 \\ iD^{\rm tot} & S^{\rm tot} & 0 \\ 0 & 0 & P^{\rm tot} \end{pmatrix}. \tag{30}$$

In the previous expressions, the off-diagonal terms correspond to the (nondissipative) Hall conductivity, and $S^{\rm tot}$, $D^{\rm tot}$ are defined as S, D in § 3.1 but with R, L, P replaced by

$$\begin{pmatrix} R^{\rm tot} \\ L^{\rm tot} \end{pmatrix} = 1 - \frac{\omega_p^2}{\omega^2}\frac{\omega}{\omega \mp \omega_B + i\omega_\perp^D}, \tag{31}$$

$$P^{\rm tot} = 1 - \frac{\omega_p^2}{\omega^2}\frac{\omega}{\omega + i\omega_\parallel^D}. \tag{32}$$

A further rotation by an angle α accounts for the misalignment between $\boldsymbol{B}$ and z and gives the dielectric tensor $\epsilon_{ij}^{\rm tot}$ in the same form as in equation (11).

We have repeated the computation of the monochromatic absorption coefficients by following the same method as in § 3.1, but using the dielectric tensor $\epsilon_{ij}^{\rm tot}$. The conductivities $\sigma_{\parallel,\perp}$ have been computed numerically for the appropriate values of B, ρ, and T.[6]

[6] The package CONDUCT.FOR developed by A. Potekhin and available at http://www.ioffe.ru/astro/conduct/condmag.html has been used.

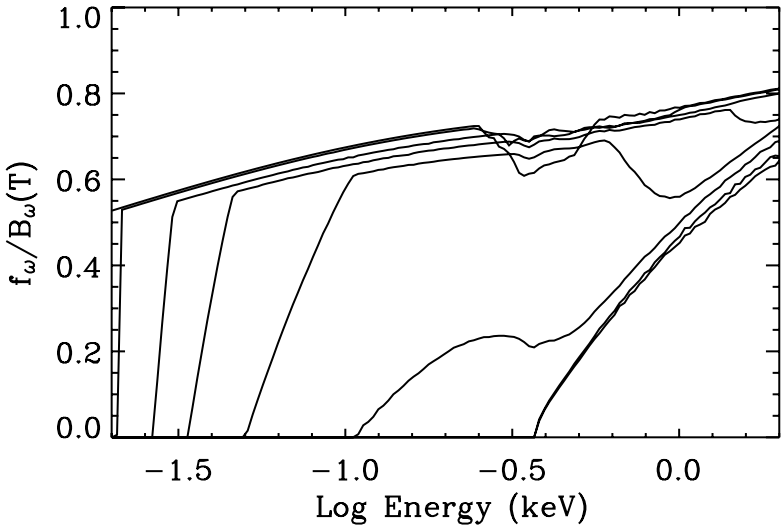

FIG. 5.—Same as in Fig. 2, but with electron-phonon damping accounted for and $B = 5 \times 10^{13}$ G, $T = 10^6$ K; curves represent, from top to bottom, $2\alpha/\pi = 0.05$, 0.2, 0.4, 0.5, 0.6, 0.7, 0.8, 0.95.

The inclusion of electron-phonon damping seriously affects the emission properties of the surface, as can be seen from Figures 3 and 5, where the angle-averaged and angle-dependent emissivity is shown.

Below $\sim$1 keV the emissivity declines quite rapidly with decreasing photon energy. There is now a strong dependence on the magnetic field strength, with the suppression being more pronounced at lower fields. This is mainly due to the role played by electron-phonon damping in the transverse plane, which is quantified by the real parts of $\sigma_{xx}^{\rm tot}$, $\sigma_{yy}^{\rm tot}$. These are $\approx\omega_p^2\omega_\perp^D/(4\pi\omega_B^2)$ and increase monotonically with decreasing B. In particular, while for $B_p \sim 5 \times 10^{13}$ G the star surface can radiate down to a few tens of eV, for $B_p \lesssim 5 \times 10^{12}$ G a sharp edge appears at $\sim$300 eV and the star surface behaves as a perfect reflector at energies below $\approx$100 eV. An absorption feature close to the cutoff energy ω_0 is now more clearly seen at $\approx$300 eV for the field strengths reported here. Contrary to the behavior of the resonant frequency ω_-, the value of the cutoff energy changes only very weakly with B (see Fig. 5). This implies that the feature survives even after integration over the entire surface has been performed (see Fig. 3). As in the cold electron gas considered in § 3.1, the emissivity is strongly dependent of the angle between the magnetic field and the surface normal (see again Fig. 5), so line-of-sight effects are expected to be important.

The different behavior produced by the inclusion of damping can be understood as follows. We start rewriting the dispersion relations (eq. [15]) in terms of the angle of refraction Θ and then compare the refractive indexes computed with and without the damping terms. We consider the case $\boldsymbol{B} \parallel z$ (i.e., $\alpha = 0$; see Melrose 1986). The ensuing equation is quadratic in n^2 and therefore simpler to solve. Results are shown in Figure 6 for $\Theta \sim 43^\circ$ and two different magnetic field strengths. As can be seen from the bottom panels of Figure 6, when collisional damping is included, the n_m^2 develop a substantial imaginary part over a wide range of energies that can easily extend up to an order of magnitude below ω_-. The region of interest is larger for decreasing field strength and/or increasing grazing angle. This causes the angle-dependent absorption feature that is seen in Figure 5 at $\log E \sim -0.6$, 0 and large α. Moreover, below a certain energy threshold both indexes develop a large imaginary part so that both propagation modes are substantially damped. Since the penetration depth is $\delta = c/[\omega{\rm Im}(n)]$, in our angle-dependent computation we neglect the contribution of modes with ${\rm Im}(n) = \lambda/(2\pi\delta) > 0.01$ (Fig. 6, *dashed line*).

Of course, the most important consequence is that the results now depend in a crucial way on the choice of the rejection limit, which in turn is only one of the aspects of the uncertainties in the physics at the vacuum/surface interface. The relevance of varying the adopted limit for rejecting on the surface emissivity is shown in Figure 7.

4. DISCUSSION

This investigation has been motivated by recent X-ray observations of RX J1856.5−3754 and RX J0720.4−3125, the two brightest among the seven isolated neutron stars discovered by *ROSAT*. In particular, detailed *Chandra* observations have convincingly shown that RX J1856.5−3754 has a featureless thermal spectrum for which a simple blackbody distribution seems to provide a better fit to X-ray data than more sophisticated atmospheric models (Burwitz et al. 2001; Drake et al. 2002). RX J1856.5−3754 has a firmly established optical counterpart (Walter & Matthews 1997; van Kerkwijk & Kulkarni 2001a), similarly to RX J0720.4−3125 (Motch & Haberl 1998; Kulkarni & van Kerkwijk 1998). Accurate spectroscopy and photometry with combined Very Large Telescope (VLT) and *Hubble Space Telescope* (*HST*) data have shown that the UV–optical energy distribution closely follows a Rayleigh-Jeans tail (van Kerkwijk & Kulkarni 2001a). However, as originally noticed by Walter & Matthews (1997), the Rayleigh-Jeans tail of the X-ray best-fitting blackbody underpredicts the optical flux by about a factor of 6 (Walter & Lattimer 2002), and this has been taken as suggestive of emission from regions on the star surface with different properties (see below). Deep *HST* observations have also revealed the presence of a bow shock nebula in Hα around RX J1856.5−3754 (van Kerkwijk & Kulkarni 2001b). Walter (2001), by means of *HST* observations, derived the proper motion and parallax of the star and obtained a distance of about 60 pc. However, this distance was shown to be in error by recent reanalysis of the same *HST* data (Kaplan et al. 2002) and of these data augmented by further observations (Walter & Lattimer 2002). These studies place the source at about 120 pc, or twice the original distance. The simultaneous determination of the distance and X-ray

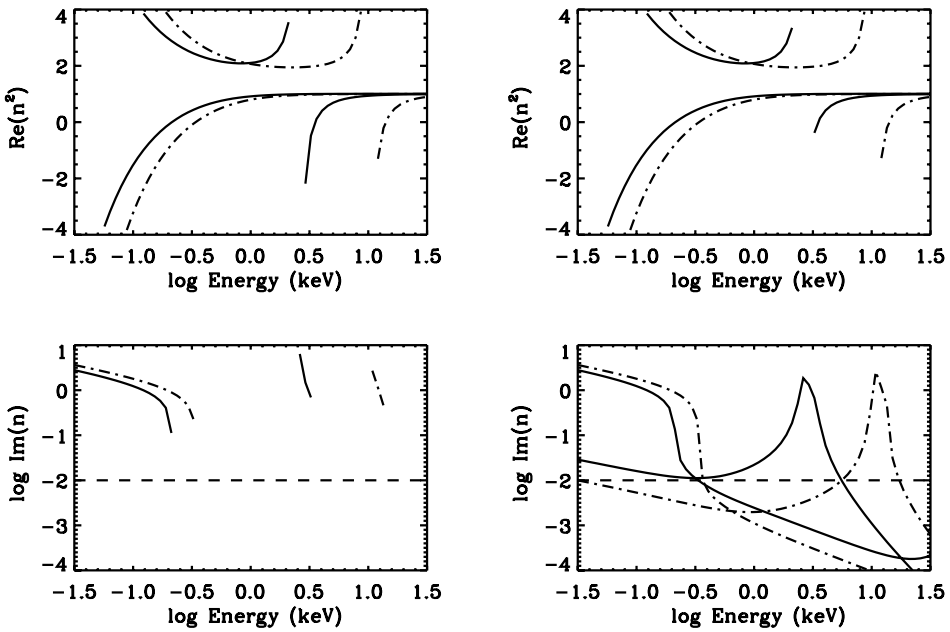

FIG. 6.—*Top*: $\mathrm{Re}(n_m^2)$ with (*right*) and without (*left*) electron-phonon damping accounted for. The refractive indexes are the solutions of the dispersion relation for $\Theta \approx 43^\circ$, $\alpha = 0$, and $B = 5 \times 10^{12}$ (*solid line*) and 5×10^{13} G (*dot-dashed line*). *Bottom*: Same for the imaginary parts of n_m. The dashed line represents our rejection criterion, $\mathrm{Im}(n) > 0.01$ (see text).

flux (under the reasonable assumption that it comes from the stellar surface) makes RX J1856.5−3754 unique in its class inasmuch as it allows a direct estimate of the radiation radius

$$R_\infty = 4.25 \left(\frac{D}{100 \text{ pc}} \right) \left(\frac{T_{\rm bb}}{60 \text{ eV}} \right)^{-2} \text{ km}. \tag{33}$$

Based on the location of RX J1856.5−3754 in front of the R CrA molecular cloud, Drake et al. (2002) have shown that their derived neutral H column density of 1×10^{20} cm^{-2} limits the distance to $\leq$170 pc. Taken at face value, the expression for the radiation radius above yields for this distance a value of at most $\sim$8.2 km. Such a figure is incompatible with current bounds on the stellar radius (as measured by an observer at radial infinity) based on theoretical investigations of the EOS of matter at ultrahigh densities (see, e.g., Lattimer & Prakash 2001), $12 \text{ km} \lesssim R_\infty \lesssim 17$ km. This discrepancy motivated the suggestion that RX J1856.5−3754 might be a strange/quark star (Haensel 2001; Xu 2002; Drake et al. 2002; Gondek-Rosińska, Kluźniak, & Stergioulas 2002).

More conventional scenarios involving a NS have been discussed in connection with RX J1856.5−3754. Pons et al. (2002) explored nonmagnetized model atmospheres with different compositions (H, He, Fe, Si-ash) in order to reproduce the emission

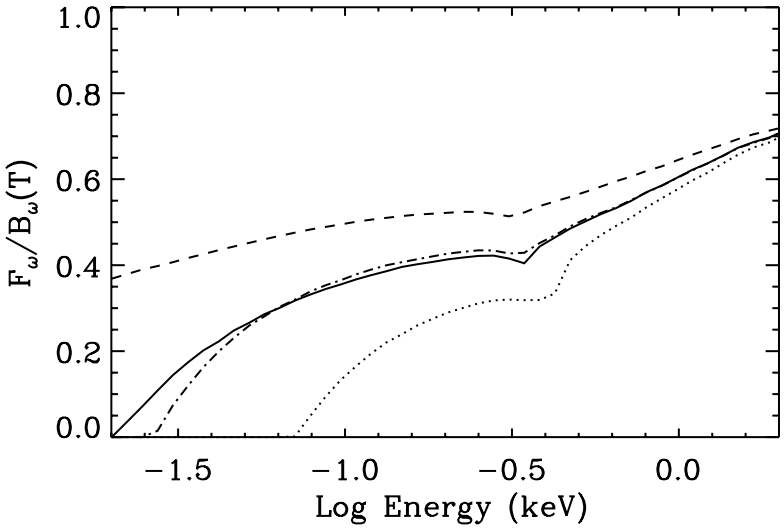

FIG. 7.—Same as in Fig. 3, but for $B_p = 5 \times 10^{13}$ G and different values of the rejection limit: $\mathrm{Im}(n) = 0.01$ (*solid line*), 0.05 (*dashed line*), and 0.005 (*dotted line*). The dot-dashed line shows the surface emissivity for the meridional temperature distribution [$\mathrm{Im}(n) = 0.01$; see the caption of Fig. 4] and is to be compared with the solid curve.

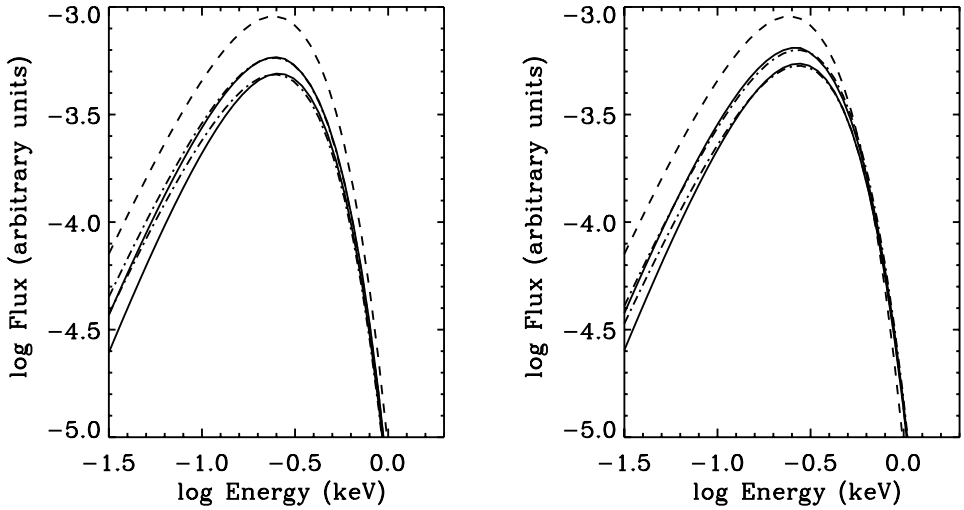

FIG. 8.—Emitted spectrum in the cold plasma limit for $B_p = 2 \times 10^{13}$ G and $T_{\rm surf} = 10^6$ K. *Left*: Uniform surface temperature. *Right*: Meridional temperature variation as defined in the caption of Fig. 4. The dashed line is the blackbody at $T_{\rm surf}$ and the dot-dashed line the blackbody that best fits the calculated spectrum in the 0.1–2 keV range. The two models shown in each panel are computed for $\omega_p = \omega_{p,0}$ (*upper solid curve*) and $2.45\omega_{p,0}$ (*lower solid curve*). Spectra are at the star surface, and no redshift correction has been applied.

properties of RX J1856.5−3754. H/He spectra are almost featureless, but they deviate substantially from a blackbody, showing an excess at higher energies. As was already noted by Campana, Mereghetti, & Sidoli (1997) and further remarked on by Pons et al. (2002), the fit with H/He atmospheric models yields a column density distance $\lesssim$10 pc for standard values of the star radius, more than 1 order of magnitude below the parallax measurement.

Pons et al. (2002) considered both a uniform thermal distribution and a two-temperature surface model. For the adopted distance of 61 pc (Walter 2001), they concluded that the apparent radius is $\approx$7–8 km for a uniform thermal distribution, which is too small for any EOSs. Owing to the reduced area of the hotter X-ray–emitting region, two-component models provide larger values for R_∞ and may also explain the excess at optical wavelengths over the best-fitting X-ray blackbody. With a revised distance of 117 pc, Walter & Lattimer (2002) argued that both the single-component heavy-element (Fe and Si) and two-component blackbody models of Pons et al. (2002) yield acceptable values for the stellar radius. In particular, they claim that a two-temperature model in which a blackbody at $T = 15$ eV is emitted by a region with an angular diameter 5 times larger than the X-ray blackbody ($T = 63$ eV) can reproduce the multiwavelength SED.

These conclusions are not without problems. Although detailed spectral calculations were announced, the present results of Walter & Lattimer (2002) rely on the assumption that the two regions on the stellar surface emit a pure blackbody spectrum. How to justify this assumption for a NS, however, remains unexplained. Moreover, the presence of a small, hot region on the star surface might be difficult to reconcile with the lack of pulsations in the X-ray flux, as stressed by Drake et al. (2002), especially in the light of the present very tight limits on the pulsed fraction of this source ($\lesssim$1.3%; Burwitz et al. 2003). All heavy-element spectra calculated by Pons et al. (2002) exhibit a variety of emission/absorption features in the soft X-ray range. No evidence for such features is present in the *Chandra* and *XMM-Newton* data.

More recently, Braje & Romani (2002) readdressed the two-temperature surface model for RX J1856.5−3754, pointing out that several effects (isothermality, magnetic smearing, rotation) may act in suppressing the spectral features from an extended atmosphere with heavy elements. In particular, they discuss in detail the role of rotation, showing that phase-dependent Doppler shifts in a rapidly rotating NS ($P \approx 1$ ms) wash out all features, leaving a nearly Planckian spectrum. Although such a short period cannot be excluded on the basis of present data, the detected periods of other thermally emitting INSs are in the range $\approx$0.1–10 s, about 2 orders of magnitude larger. In the Braje & Romani (2002) picture the X-ray–emitting region is kept warm by external heating, and the genuine surface temperature should correspond to the cooler blackbody at $T \sim 15$ eV. A millisecond period appears hardly compatible with the star's age of, as implied by conventional cooling curves, $\approx 10^6$ yr. Furthermore, the energetics of the bow shock nebula implies $P = 4.6(B/10^8\ {\rm G})^{1/2}$ ms. A millisecond spin period therefore necessarily demands a very low field star. Such a low field seems hard to reconcile with the limit on the age derived again from the bow shock energetics, $(B/10^{12}\ {\rm G})(\tau/10^6\ {\rm yr}) \sim 3$–4.

Although two-temperature models appear promising in explaining the multiwavelength SED of RX J1856.5−3754, no conclusive evidence has been provided yet that a near-blackbody, featureless spectrum can be emitted by an extended atmosphere covering the stellar crust. An alternative possibility, originally suggested by Burwitz et al. (2001; see also Burwitz et al. 2003) and further explored here, is that RX J1856.5−3754 may be a solid-surface NS. If this is the case, a severe reduction in the surface emissivity has to be expected at energies below the plasma frequency, according to the analysis of Lenzen & Trümper (1978) and B80. The bare NS model may ease the radiation radius problem. In fact, denoting with f_E the ratio of emitted to blackbody power and assuming emission from the entire star surface, the value of R_∞ now contains an additional $f_E^{-1/2}$ factor with respect to that given by equation (33). As expected, the reduced surface emissivity acts precisely in the same way as a reduced emitting area, requiring a larger star radius. In order to represent a viable option, the bare NS picture must conform to three basic requirements: (1) the conditions for the appearance of a solid phase should be met, at least within the present uncertainties; (2) the X-ray spectrum

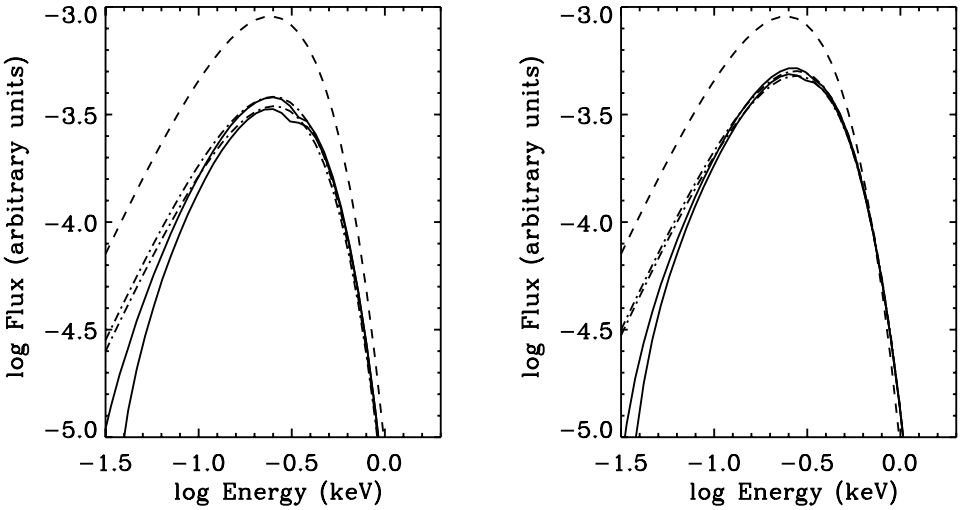

FIG. 9.—Same as in Fig. 8, but for the case with electron-phonon damping. The two models shown in each panel are computed for $B_p = 2 \times 10^{13}$ and 5×10^{13} G; here $\omega_p = \omega_{p,0}$, and other details are as in Fig. 8.

emitted by the surface should be very close to blackbody in the 0.1–2 keV range to match *Chandra*/*XMM* observations; and (3) quite low values of f_E ($\approx$0.1) should be possible for R_∞ to be in the range allowed by current EOSs.

In the absence of a measured period and period derivative, the magnetic field of RX J1856.5−3754 is still a mystery. Given a surface temperature of $\sim$70 eV, the magnetic field of RX J1856.5−3754 should be in excess of 10^{13} G, more probably at least $(3-5) \times 10^{13}$ G, for its surface layers to be in the form of condensed iron (see § 2 and Fig. 1). Although rather high, such a field strength is well below the magnetar range and is noticeably shared by another *ROSAT* INS: RX J0720.4−3125 (Zane et al. 2002). Thus, although no definite conclusion can be drawn, the possibility that RX J1856.5−3754 is a solid-surface NS is real.

In the light of the results presented in § 3, the remaining two points are much more of an issue. When computed accounting only for the cold electron gas (§ 3.1), spectra show indeed only small departures from a blackbody in the 0.1–2 keV band. A typical example is shown in Figure 8, where the computed spectra are plotted together with the best-fitting blackbody (again in the 0.1–2 keV range) for two different temperature distributions on the star surface. Deviations from a blackbody are below 15%–20%, and this would make it possible to reasonably fit *Chandra* data. The value of f_E depends on the magnetic field and the surface density (see Fig. 4). In order to reach $f_E \sim 0.3$ (which produces an increase in radius of $\sim$2), one must invoke a density $\approx$50 times larger than the zero-pressure value given by equation (1). Although the latter is only an approximation, such a large departure might not be realistic. For $\rho \sim \rho_s$, the predicted increase in radius is $\sim$15%, which is insufficient to reconcile the radiation radius with canonical theoretical predictions, at least when viewing angle effects are neglected (see also Thoma et al. 2003).

These models are, however, unrealistic. The cold electron gas assumption is a poor approximation at low energies where damping by electron-lattice interactions becomes progressively more important. When collisional damping (computed following Potekhin 1999) is accounted for, we found that the surface emissivity is substantially depressed below $\approx$1 keV with respect to the cold electron gas case. At low fields ($\lesssim 5 \times 10^{12}$ G) virtually no emission is expected at energies below $\approx$0.5 keV, while the decline at low energies is not so sharp for $B \gtrsim 10^{13}$ G (see Fig. 3 and the discussion at the end of § 3.2). The emerging spectrum is shown in Figure 9 for two representative values of the polar magnetic field. Despite the spectra deviating quite strongly from a blackbody distribution at low energies, the fit with a blackbody in the 0.1–2 keV range is still acceptable, with maximal deviations typically below 20%. At the lower field strength shown in Figure 9 ($B_p = 2 \times 10^{13}$ G), $f_E \sim 0.35$, which would imply a radius larger than the pure blackbody radius by about a factor of 2. This is definitely larger than what is predicted by the cold electron gas models with $\rho = \rho_s$ and may be enough to provide an acceptable value of the stellar radius. However, at least for the uniform temperature distribution, for such values of the polar field the absorption feature around $\omega_0 \sim 300$ eV is clearly present in the spectrum (see again Fig. 9). The feature is not so pronounced at larger fields, but f_E becomes higher ($\sim$0.45), making the radius a problem again. One has also to bear in mind that the spectra shown in Figure 9 have been computed for a fixed rejection threshold. As Figure 7 shows, the choice of this parameter (even within a factor of a few) has a crucial influence on the shape of emitted spectrum.

Apart from the considerable uncertainties in current modeling of the physics governing the phase transition (see § 2 and Lai 2001 for a more detailed discussion), we remind the reader that our spectra have been computed under a number of simplifying assumptions. A thorough discussion of the limitations of this kind of approach can be found in B80. The greatest uncertainties arise because of the assumption of a sharp transition from vacuum to a smooth metallic surface, neglecting the effects of the macroscopic surface structure. We assumed that the surface is made of pure iron, but different chemical compositions, or the presence of impurities in the iron surface, may change the results. Inside the star we neglect the role of bound electrons and further effects produced by the dissipation of those waves that are rapidly attenuated within a skin penetration depth.

Finally, from a different perspective and regarding the possible application of the present work, we point out that the calculation of the complex refractive indexes below the plasma frequency presented here may substantially contribute to the determination of the photon thermal conductivities of ultramagnetized NSs. These are, in turn, important for the accurate calculation of the thermal structure and cooling of these objects (see Potekhin et al. 2003).

We are deeply indebted to A. Potekhin for a critical reading of the manuscript, for his comments and suggestions, and for pointing out the relevance of this work in connection with photon thermal conductivity computations. We thank M. Chieregato and K. Wu for many helpful discussions during the earlier stages of this work. We also acknowledge an anonymous referee whose penetrating questions and comments greatly improved an earlier version of this paper. This work was partially supported by the Italian Ministry for Education, University and Research (MIUR) under grant COFIN-2002-027145. J. J. D. was supported by NASA contract NAS8-39073 to the *Chandra* X-Ray Center.

APPENDIX

EFFECTS OF VACUUM POLARIZATION

In §§ 3.1 and 3.2 the NS surface emissivity has been computed under the assumption that radiation propagates in vacuo outside the star and neglecting the magnetized vacuum birefringence and polarization properties. At the field strengths we consider ($B \lesssim B_{\rm QED} \equiv m_e c^3/\hbar e \simeq 4.4 \times 10^{13}$ G), this has little effect on the vacuum refractive index for which deviations from unity are very small (see below). Yet, radiation propagating in the magnetized vacuum has two well-defined polarization states, corresponding to the ordinary (O) and extraordinary (X) modes, even if the two modes propagate at very nearly the same speed ($n_O \simeq n_X \simeq 1$). Therefore, in principle the entire formalism should be generalized to account for nonscalar absorption and emission coefficients. In order to quantify this effect, we proceed as follows. We maintain the same Cartesian frame introduced in § 3.1, and, at fixed magnetic colatitude θ, we first consider incident radiation with polarization mode s (here and in the following s stands for either O or X). The vacuum dielectric tensor is expressed as (e.g., Mészáros 1992; Heyl & Hernquist 1997)

$$\epsilon_{ij}^{\rm vac} = \begin{pmatrix} a + q\sin^2\alpha & 0 & q\sin\alpha\cos\alpha \\ 0 & a & 0 \\ q\sin\alpha\cos\alpha & 0 & a + q\cos^2\alpha \end{pmatrix}. \tag{A1}$$

Suitable expressions for a and q have been given by Ho & Lai (2003). In the weak-field limit $B \lesssim B_{\rm QED}$ they are

$$a \approx 1 - 2\delta_V, \qquad q \approx 7\delta_V, \qquad \delta_V = \frac{\alpha_F}{45\pi} b_V^2, \tag{A2}$$

where $\alpha_F = 1/137$ and $b_V = B/B_{\rm QED}$, while for $B \gtrsim B_{\rm QED}$ they are

$$a \approx 1 + \frac{\alpha_F}{45\pi}\left[1.195 - \frac{2}{3}\ln b_V - \frac{1}{b_V}(0.8553 + \ln b_V) - \frac{1}{2b_V^2}\right],$$

$$q \approx -\frac{\alpha_F}{45\pi}\left[-\frac{2}{3}b_V + 1.272 - \frac{1}{b_V}(0.3070 + \ln b_V) - 0.7003\frac{1}{b_V^2}\right]. \tag{A3}$$

The two unit propagation eigenmodes are

$$\begin{aligned} \boldsymbol{e}_X &= \frac{\boldsymbol{k}\times\boldsymbol{b}}{\sin\delta} = \frac{1}{\sin\delta}(\cos\alpha\sin i\sin\beta, -\cos\alpha\sin i\cos\beta + \sin\alpha\cos i, -\sin\alpha\sin i\cos\beta), \\ \boldsymbol{e}_O &= \frac{\boldsymbol{b} - n_O^2\cos\delta\boldsymbol{k}}{\sqrt{1 + n_O^2(n_O^2-2)\cos^2\delta}} \\ &= \frac{1}{\sqrt{1 + n_O^2(n_O^2-2)\cos^2\delta}}\left(\sin\alpha - n_O^2\cos\delta\sin i\cos\beta, -n_O^2\cos\delta\sin i\sin\beta,\ \cos\alpha - n_O^2\cos\delta\cos i\right), \end{aligned} \tag{A4}$$

with $\cos\delta \equiv \boldsymbol{k}\cdot\boldsymbol{b} = \cos i\cos\alpha + \sin i\sin\alpha\cos\beta$. Series expansions for the refractive indexes of the two modes have been given by Heyl & Hernquist (1997). In the weak-field limit it is

$$n_O \approx 1 - \frac{\alpha_F}{4\pi}\sin^2\delta\left[\frac{16}{3}B_4 b_V^2 + \frac{64}{5}B_6 b_V^4 + O(b_V^6)\right] + O\left[\left(\frac{\alpha_F}{4\pi}\right)^2\right],$$

$$n_X \approx 1 + \frac{\alpha_F}{4\pi}\sin^2\delta\left[\frac{14}{45}b_V^2 - 0.53(6B_6 - 5B_4)b_V^4 + O(b_V^6)\right] + O\left[\left(\frac{\alpha_F}{4\pi}\right)^2\right], \tag{A5}$$

while the corresponding expressions in the strong-field limit are

$$n_O \approx 1 + \frac{\alpha_F}{4\pi}\sin^2\delta\left[\frac{2}{3} - (\ln b_V + 1 - \ln\pi)\frac{1}{b_V} + O\left(\frac{1}{b_V^2}\right)\right] + O\left[\left(\frac{\alpha_F}{4\pi}\right)^2\right],$$

$$n_X \approx 1 + \frac{\alpha_F}{4\pi}\sin^2\delta\left[\frac{2}{3}b_V - \left(8\ln A - \frac{1}{3} - \frac{2}{3}\gamma_{\rm E}\right) - \left(\ln\pi + \frac{\pi^2}{18} - 2 - \ln b_V\right)\frac{1}{b_V} + O\left(\frac{1}{b_V^2}\right)\right] + O\left[\left(\frac{\alpha_F}{4\pi}\right)^2\right]. \quad \text{(A6)}$$

Here B_n are the Bernoulli numbers, $\ln A \simeq 0.2488$, and $\gamma_{\rm E}$ is the Euler constant.

At the surface an incident electromagnetic wave, described by its electric field $\boldsymbol{E}_s$, wavevector $\boldsymbol{k}_s$, and refraction index n_s, is partly reflected and partly refracted. Because of the birefringence of both media (the vacuum and the solid star crust), this gives rise to two refracted and two reflected waves. The latter are again either X or O polarized with electric field $\boldsymbol{E}''_{s,r}$ where, once more, $r = O, X$.[7] In the following we ignore the small ($O|n_O - n_X|$) difference in the angle of reflection and assume that the two reflected waves propagate in the same direction fixed by the angles i, $\beta + \pi$.

Since we are not interested in studying the polarization state of the emergent radiation, but only its spectral distribution, it is useful to introduce the two quantities

$$\rho_{\omega,s} \equiv \frac{\sum_r \left|\boldsymbol{E}''_{s,r}\right|^2}{|\boldsymbol{E}_s|^2}, \quad \text{(A7)}$$

which represent the ratios between the reflected and incident intensities when the incident wave is either X or O polarized (intensities are proportional to squared amplitudes of the electric fields to first approximation[8]). The absorption coefficients corresponding to the two incident modes are $\alpha_{\omega,s} = 1 - \rho_{\omega,s}$, and, again, from Kirchhoff's law we get the total emissivity $j_\omega = \alpha_\omega B_\omega(T)$, where $\alpha_\omega = (\alpha_{\omega,O} + \alpha_{\omega,X})/2$. The monochromatic and total fluxes are computed again by performing the integrals in equations (9) and (10).

Inside the star, each refracted wave splits into an ordinary ($\boldsymbol{E}'_{s,1}, \boldsymbol{k}'_{s,1}$) and an extraordinary ($\boldsymbol{E}'_{s,2}, \boldsymbol{k}'_{s,2}$) mode. In order to compute $\rho_{\omega,s}$, we then proceed exactly as discussed in § 3.1 by solving the dispersion relation and computing the refractive index n_i, $i = 1, 2$, for the two refracted modes. Since n_s now explicitly appears in Snell's law ($n = n_s \sin i/\sin\Theta$), we have to solve the dispersion relation twice,

$$n^4\left(P + v\sin^2\alpha\right) + n^2\left(gv - 2PS + u\sin^2\alpha\right) + PRL + gu = n_s \sin i \sin(2\alpha)\cos\beta\left(n^2 - n_s^2\sin^2 i\right)^{1/2}\left(u + n^2 v\right), \quad \text{(A8)}$$

where $g = n_s^2\sin^2 i[1 - \sin^2\alpha(1 + \cos^2\beta)]$ and all other quantities are the same as in equation (15).

Once the refractive indexes are known, we solve the wave equations $\lambda_{s,ij}(n_m)E'_{s,mj} = 0$, where $E'_{s,mj}$ are the Cartesian components of $\boldsymbol{E}'_{s,m}$, obtaining the two ratios $E'_{s,mx}/E'_{s,mz}$ and $E'_{s,my}/E'_{s,mz}$. The resulting expressions are

$$\begin{aligned}\frac{E'_{s,mx}}{E'_{s,mz}} \equiv a_m = &\Bigg[-n_m^2 n_s^2\sin^2 i\sin\beta\cos\beta - iDn_s^2\sin^2 i\cos\alpha + iDn_s\cos\beta\sin\alpha\sin i\sqrt{n_m^2 - n_s^2\sin^2 i} \\ &- n_s\sin\beta(P - S)\sin\alpha\cos\alpha\sin i\sqrt{n_m^2 - n_s^2\sin^2 i} + n_s^2\sin^2 i\sin\beta\cos\beta\left(P\cos^2\alpha + S\sin^2\alpha\right) + iD\cos\alpha P\Bigg] \\ &\times\Bigg\{-n_m^2 n_s\sin i\sqrt{n_m^2 - n_s^2\sin^2 i}\sin\beta + iD\sin\alpha n_m^2 - iDn_s^2\sin\alpha\sin^2 i\cos^2\beta - iDn_s\cos\alpha\cos\beta\sin i\sqrt{n_m^2 - n_s^2\sin^2 i} \\ &+ n_s\sin i\sqrt{n_m^2 - n_s^2\sin^2 i}\left[\sin\beta S + \sin\beta\sin^2\alpha(P - S)\right] - (P - S)n_s^2\sin\alpha\cos\alpha\sin^2 i\sin\beta\cos\beta - iD\sin\alpha P\Bigg\}^{-1},\end{aligned} \quad \text{(A9)}$$

$$\frac{E'_{m,y}}{E'_{m,z}} \equiv b_m = \left[a_m\left(n_s^2\sin^2 i\sin\beta\cos\beta - iD\cos\alpha\right) + n_s\sin\beta\sin i\sqrt{n_m^2 - n_s^2\sin^2 i} + iD\sin\alpha\right]\left(n_s^2\sin^2\beta\sin^2 i - n_m^2 + S\right)^{-1}. \quad \text{(A10)}$$

[7] Strictly speaking, the reflected wave is not necessarily linearly polarized; however, it will separate in the two allowed polarization states after propagating a distance $l_v \approx 2\pi c/(\omega|n_O - n_X|) \approx 10^{-4}$ cm for X-ray energies and $B \approx B_{\rm QED}$ (see, e.g., Chanan, Novick, & Silver 1979; Mészáros 1992). The total intensity of the reflected radiation will be the same far away from the source, despite the change in the polarization state.

[8] We neglect deviations between the directions of the two reflected waves and that of the corresponding time-averaged energy fluxes, the latter defined by the Poynting vectors.

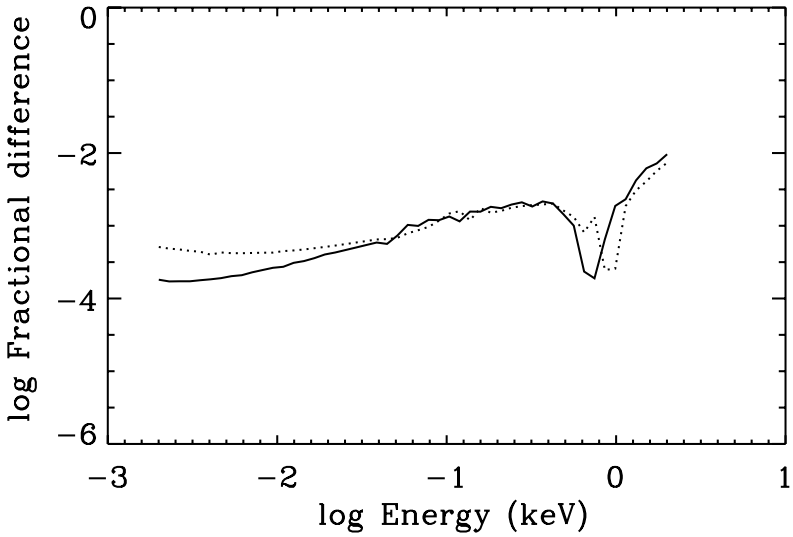

FIG. 10.—Fractional difference in the computed values of $F_\omega/B_\omega(T)$ with and without vacuum polarization taken into account (see the Appendix) at different energies. Solid and dotted lines are for $B_p = 3 \times 10^{13}$ and 6×10^{13} G, respectively.

The generalization of the Fresnel equations (e.g., Jackson 1975 and B80) to the present case gives

$$n_s E_{s\perp} + \sum_r n_r E''_{s,r\perp} = n_s \sum_m \mathcal{B}_m E'_{s,mz}, \qquad n_s E_{s\perp} - \sum_r n_r E''_{s,r\perp} = \sum_m w_m \mathcal{B}_m E'_{s,mz},$$
$$E_{s\parallel} - \sum_r E''_{s,r\parallel} = \sum_m \frac{\mathcal{A}_m}{\cos i} E'_{s,mz}, \qquad E_{s\parallel} + \sum_r E''_{s,r\parallel} = \sum_m \frac{\mathcal{C}_m}{\sin i} E'_{s,mz}. \tag{A11}$$

In the previous expressions the components of $\boldsymbol{E}_s$, $\boldsymbol{E}''_{s,r}$ are parallel and orthogonal to the plane of incidence, $w_m = (n_m^2 - n_s^2 \sin^2 i)^{1/2}/\cos i$, $\mathcal{A}_m = b_m \sin\beta - a_m \cos\beta$, $\mathcal{B}_m = b_m \cos\beta + a_m \sin\beta$, $\mathcal{C}_m = a_m \epsilon'_{31} + b_m \epsilon'_{32} + \epsilon'_{33}$, and $\epsilon'_{ik}\epsilon^{\rm vac}_{kj} = \epsilon_{ij}$. The components of the electric field of the incident and reflected waves can be expressed in terms of the amplitudes E_s and $E''_{s,r}$ as

$$E_{s\perp} = f_s E_s, \qquad E_{s\parallel} = g_s E_s, \qquad E_{s,r\perp} = f''_r E''_{s,r}, \qquad E_{s,r\parallel} = g''_r E''_{s,r}, \tag{A12}$$

where

$$f_X = \cos\gamma, \qquad g_X = \sin\gamma, \qquad \cos\gamma = \frac{-\cos\alpha \sin i + \cos\beta \sin\alpha \cos i}{\sin\delta},$$
$$f_O = \cos\xi, \qquad g_O = \sin\xi, \qquad \cos\xi = \frac{\sin\beta \sin\alpha}{\sqrt{1 + n_O^2(n_O^2 - 2)\cos^2\delta}}. \tag{A13}$$

The expressions for f''_X, f''_O, g''_X, g''_O are obtained from the previous ones by replacing β with $\beta + \pi$.

Inserting equation (A12) into equation (A11) finally gives the amplitude ratios

$$\frac{E''_{s,O}}{E_s} = -\left\{\left[f_s \frac{\overline{w}_2 - 1}{(\overline{w}_2 - \overline{w}_1)\mathcal{B}_1} - g_s \frac{\mathcal{C}_2 \cos i - \mathcal{A}_2 \sin i}{\mathcal{A}_1\mathcal{C}_2 - \mathcal{A}_2\mathcal{C}_1}\right](\overline{Q}_s - Q_X)\right\}\left\{\left[\frac{n_O}{n_s} f''_O \frac{\overline{w}_2 + 1}{(\overline{w}_2 - \overline{w}_1)\mathcal{B}_1} + g''_O \frac{\mathcal{C}_2 \cos i + \mathcal{A}_2 \sin i}{\mathcal{A}_1\mathcal{C}_2 - \mathcal{A}_2\mathcal{C}_1}\right](Q_O - Q_X)\right\}^{-1},$$
$$\frac{E''_{s,X}}{E_s} = -\left\{\left[f_s \frac{\overline{w}_2 - 1}{(\overline{w}_2 - \overline{w}_1)\mathcal{B}_1} - g_s \frac{\mathcal{C}_2 \cos i - \mathcal{A}_2 \sin i}{\mathcal{A}_1\mathcal{C}_2 - \mathcal{A}_2\mathcal{C}_1}\right](\overline{Q}_s - Q_O)\right\}\left\{\left[\frac{n_X}{n_s} f''_X \frac{\overline{w}_2 + 1}{(\overline{w}_2 - \overline{w}_1)\mathcal{B}_1} + g''_X \frac{\mathcal{C}_2 \cos i + \mathcal{A}_2 \sin i}{\mathcal{A}_1\mathcal{C}_2 - \mathcal{A}_2\mathcal{C}_1}\right](Q_X - Q_O)\right\}^{-1}, \tag{A14}$$

where $\overline{w}_m = w_m/n_s$ and

$$Q_X = \left[\frac{n_X}{n_s} f''_X \frac{\overline{w}_1 + 1}{(\overline{w}_1 - \overline{w}_2)\mathcal{B}_2} + g''_X \frac{\mathcal{C}_1 \cos i + \mathcal{A}_1 \sin i}{\mathcal{A}_2\mathcal{C}_1 - \mathcal{A}_1\mathcal{C}_2}\right]\left[\frac{n_X}{n_s} f''_X \frac{\overline{w}_2 + 1}{(\overline{w}_2 - \overline{w}_1)\mathcal{B}_1} + g''_X \frac{\mathcal{C}_2 \cos i + \mathcal{A}_2 \sin i}{\mathcal{A}_1\mathcal{C}_2 - \mathcal{A}_2\mathcal{C}_1}\right]^{-1},$$
$$Q_O = \left[\frac{n_O}{n_s} f''_O \frac{\overline{w}_1 + 1}{(\overline{w}_1 - \overline{w}_2)\mathcal{B}_2} + g''_O \frac{\mathcal{C}_1 \cos i + \mathcal{A}_1 \sin i}{\mathcal{A}_2\mathcal{C}_1 - \mathcal{A}_1\mathcal{C}_2}\right]\left[\frac{n_O}{n_s} f''_O \frac{\overline{w}_2 + 1}{(\overline{w}_2 - \overline{w}_1)\mathcal{B}_1} + g''_O \frac{\mathcal{C}_2 \cos i + \mathcal{A}_2 \sin i}{\mathcal{A}_1\mathcal{C}_2 - \mathcal{A}_2\mathcal{C}_1}\right]^{-1},$$
$$\overline{Q}_s = \left[f_s \frac{\overline{w}_1 - 1}{(\overline{w}_1 - \overline{w}_2)\mathcal{B}_2} - g_s \frac{\mathcal{C}_1 \cos i - \mathcal{A}_1 \sin i}{\mathcal{A}_2\mathcal{C}_1 - \mathcal{A}_1\mathcal{C}_2}\right]\left[f_s \frac{\overline{w}_2 - 1}{(\overline{w}_2 - \overline{w}_1)\mathcal{B}_1} - g_s \frac{\mathcal{C}_2 \cos i - \mathcal{A}_2 \sin i}{\mathcal{A}_1\mathcal{C}_2 - \mathcal{A}_2\mathcal{C}_1}\right]^{-1}. \tag{A15}$$

Again, when only one refracted wave (labeled "1" for convenience) survives, the previous calculation yields ($f_s'', g_s'' \neq 0$)

$$\frac{E''_{s,O}}{E_s} = \left(\frac{n_s}{n_X} \frac{f_s}{f''_X} \frac{\overline{w}_1 - 1}{\overline{w}_1 + 1} + \frac{g_s}{g''_X} \frac{\mathcal{C}_1 \cos i - \mathcal{A}_1 \sin i}{\mathcal{C}_1 \cos i + \mathcal{A}_1 \sin i} \right) \left(\frac{g''_O}{g''_X} - \frac{n_O}{n_X} \frac{f''_O}{f''_X} \right)^{-1},$$
$$\frac{E''_{s,X}}{E_s} = \left(\frac{n_s}{n_O} \frac{f_s}{f''_O} \frac{\overline{w}_1 - 1}{\overline{w}_1 + 1} + \frac{g_s}{g''_O} \frac{\mathcal{C}_1 \cos i - \mathcal{A}_1 \sin i}{\mathcal{C}_1 \cos i + \mathcal{A}_1 \sin i} \right) \left(\frac{g''_X}{g''_O} - \frac{n_X}{n_O} \frac{f''_X}{f''_O} \right)^{-1}, \quad \text{(A16)}$$

from which $\rho_{\omega,s}$ follows. Similar expressions can be derived in the case in which either f_s'' or g_s'' vanishes.

The absorption coefficients $\alpha_{\omega,s} = 1 - \rho_{\omega,s}$ have been computed numerically in the relevant angular ranges following the procedure outlined above, and the results have been used to evaluate j_ω and f_ω (see eq. [9]). The quantity $f_\omega / B_\omega(T)$ has then been compared with its value computed by neglecting vacuum polarization. We repeated the comparison for different values of magnetic field; some examples are shown in Figure 10. Fractional corrections turn out to be always negligible, being at most $\sim 10^{-2}$ below 2 keV. Vacuum corrections enter the dielectric tensor via the two quantities $a - 1$ and q, and, even for $B_p \sim 5 \times 10^{13}$ G, the largest value we consider in our model, it is $|a - 1| \approx q \approx 10^{-4}$. The corresponding deviation of the refractive index from unity in the vacuum outside the star is indeed negligible. Therefore, when we compute the total reflectivity we are superimposing two incident modes perpendicular to each other. Choosing them in the plane perpendicular and parallel to the plane of incidence or, as in this case, with ordinary and extraordinary polarization is not important as long as they travel at nearly the same speed.

REFERENCES

Baiko, D. A., Kaminker, A. D., Potekhin, A. Y., & Yakovlev, D. G. 1998, Phys. Rev. Lett., 81, 5556
Bignami, G. F., & Caraveo, P. A. 1996, ARA&A, 34, 331
Braje, T. M., & Romani, R. W. 2002, ApJ, 580, 1043
Brinkmann, W. 1980, A&A, 82, 352 (B80)
Burwitz, V., et al. 2001, A&A, 379, L35
———. 2003, A&A, 399, 1109
Campana, S., Mereghetti, S., & Sidoli, L. 1997, A&A, 320, 783
Chanan, G. A., Novick, R., & Silver, E. H. 1979, ApJ, 228, L71
Cropper, M., et al. 2001, A&A, 365, L302
Drake, J. J., et al. 2002, ApJ, 572, 996
Flowers, E., & Itoh, N. 1976, ApJ, 206, 218
Gondek-Rosińska, D., Kluźniak, W., & Stergioulas, N. 2002, preprint (astro-ph/0206470)
Greenstein, G., & Hartke, G. J. 1983, ApJ, 271, 283
Greiveldinger, C., et al. 1996, ApJ, 465, L35
Haberl, F., et al. 1997, A&A, 326, 662
———. 2003, A&A, 403, L19
Haensel, P. 2001, A&A, 380, 186
Halpern, J. P., & Wang, F. Y.-H. 1997, ApJ, 477, 905
Hernquist, L. 1984, ApJS, 56, 325
Heyl, J. S., & Hernquist, L. 1997, J. Phys. A, 30, 6485
Ho, W. C. G., & Lai, D. 2003, MNRAS, 338, 233
Jackson, J. D. 1975, Classical Electrodynamics (New York: Wiley)
Jones, P. B. 1986, MNRAS, 218, 477
Kaminker, A. D., & Yakovlev, D. G. 1981, Theor. Math. Phys., 49, 1012
Kaplan, D. L., van Kerkwijk, M. H., & Anderson, J. 2002, ApJ, 571, 447
Kulkarni, S. R., & van Kerkwijk, M. H. 1998, ApJ, 507, L49
Lai, D. 2001, Rev. Mod. Phys., 73, 629
Lai, D., & Salpeter, E. E. 1997, ApJ, 491, 270
Lattimer, J. M., & Prakash, M. 2001, ApJ, 550, 426
Lenzen, R., & Trümper, J. 1978, Nature, 271, 216
Marion, J. B. 1965, Classical Electromagnetic Radiation (New York: Academic)
Marshall, H. L., & Schulz, N. S. 2002, ApJ, 574, 377
Melrose, D. B. 1986, Instabilities in Space and Laboratory Plasmas (Cambridge: Cambridge Univ. Press)
Mészáros, P. 1992, High-Energy Radiation from Magnetized Neutron Stars (Chicago: Univ. Chicago Press)
Motch, C. 2001, in AIP Conf. Proc. 599, X-Ray Astronomy: Stellar Endpoints, AGN, and the Diffuse X-Ray Background, ed. N. E. White, G. Malaguti, & G. G. C. Palumbo (New York: Melville), 244
Motch, C., & Haberl, F. 1998, A&A, 333, L59
Neuhauser, D., Koonin, S. E., & Langanke, K. 1987, Phys. Rev. A, 36, 4163
Paerels, F., et al. 2001, A&A, 365, L298
Pavlov, G. G., & Zavlin, V. E. 2000, ApJ, 529, 1011
Pavlov, G. G., et al. 2001, ApJ, 552, L129
Pons, J. A., et al. 2002, ApJ, 564, 981
Possenti, A., Mereghetti, S., & Colpi, M. 1996, A&A, 313, 565
Potekhin, A. Y. 1999, A&A, 351, 787
Potekhin, A. Y., Yakovlev, D. G., Chabrier, G., & Gnedin, O. Y. 2003, ApJ, 594, 404
Rajagopal, M., Romani, R. W., & Miller, M. C. 1997, ApJ, 479, 347
Ransom, S. M., Gaensler, B. M., & Slane, P. O. 2002, ApJ, 570, L75
Shibanov, Yu. A., Zavlin, V. E., Pavlov, G. G., & Ventura, J. 1992, A&A, 266, 313
Taylor, J. H., Manchester, R. N., & Lyne, A. G. 1993, ApJS, 88, 529
Thoma, M. H., Trümper, J., & Burwitz, V. 2003, preprint (astro-ph/0305249)
Treves, A., Turolla, R., Zane, S., & Colpi, M. 2000, PASP, 112, 297
van Kerkwijk, M. H., & Kulkarni, S. R. 2001a, A&A, 378, 986
———. 2001b, A&A, 380, 221
Walter, F. M. 2001, ApJ, 549, 433
Walter, F. M., & Lattimer, J. 2002, ApJ, 576, L145
Walter, F. M., & Matthews, L. D. 1997, Nature, 389, 358
Xu, R. X. 2002, ApJ, 570, L65
Yakovlev, D. G. 1984, Ap&SS, 98, 37
Yakovlev, D. G., & Urpin, V. A. 1980, Soviet Astron., 24, 303
Zampieri, L., et al. 2001, A&A, 378, L5
Zane, S., Turolla, R., & Drake, J. J. 2004, in High Resolution X-Ray Spectroscopy with *XMM-Newton* and *Chandra*, in press (astro-ph/0302197)
Zane, S., et al. 2002, MNRAS, 334, 345
Ziman, J. M. 1978, Electrons and Phonons (Oxford: Oxford Univ. Press)